

# Planck intermediate results. XLII. Large-scale Galactic magnetic fields

Planck Collaboration: R. Adam<sup>66</sup>, P. A. R. Ade<sup>78</sup>, M. I. R. Alves<sup>86, 8, 51</sup>, M. Ashdown<sup>60, 4</sup>, J. Aumont<sup>51</sup>, C. Baccigalupi<sup>76</sup>, A. J. Banday<sup>86, 8</sup>, R. B. Barreiro<sup>56</sup>, N. Bartolo<sup>25, 57</sup>, E. Battaner<sup>88, 89</sup>, K. Benabed<sup>52, 85</sup>, A. Benoit-Lévy<sup>20, 52, 85</sup>, J.-P. Bernard<sup>86, 8</sup>, M. Bersanelli<sup>28, 42</sup>, P. Bielewicz<sup>72, 8, 76</sup>, L. Bonavera<sup>56</sup>, J. R. Bond<sup>7</sup>, J. Borrill<sup>11, 81</sup>, F. R. Bouchet<sup>52, 79</sup>, F. Boulanger<sup>51</sup>, M. Bucher<sup>1</sup>, C. Burigana<sup>41, 26, 43</sup>, R. C. Butler<sup>41</sup>, E. Calabrese<sup>83</sup>, J.-F. Cardoso<sup>65, 1, 52</sup>, A. Catalano<sup>66, 63</sup>, H. C. Chiang<sup>22, 5</sup>, P. R. Christensen<sup>73, 31</sup>, L. P. L. Colombo<sup>19, 58</sup>, C. Combet<sup>66</sup>, F. Couchot<sup>62</sup>, B. P. Crill<sup>58, 9</sup>, A. Curto<sup>56, 4, 60</sup>, F. Cuttaia<sup>41</sup>, L. Danese<sup>76</sup>, R. J. Davis<sup>59</sup>, P. de Bernardis<sup>27</sup>, A. de Rosa<sup>41</sup>, G. de Zotti<sup>38, 76</sup>, J. Delabrouille<sup>1</sup>, C. Dickinson<sup>59</sup>, J. M. Diego<sup>56</sup>, K. Dolag<sup>87, 69</sup>, O. Doré<sup>58, 9</sup>, A. Ducout<sup>52, 49</sup>, X. Dupac<sup>33</sup>, F. Elsner<sup>20, 52, 85</sup>, T. A. Enßlin<sup>69</sup>, H. K. Eriksen<sup>54</sup>, K. Ferrière<sup>86, 8</sup>, F. Finelli<sup>41, 43</sup>, O. Forni<sup>86, 8</sup>, M. Frailis<sup>40</sup>, A. A. Fraisse<sup>22</sup>, E. Franceschi<sup>41</sup>, S. Galeotta<sup>40</sup>, K. Gangal<sup>1</sup>, T. Ghosh<sup>51</sup>, M. Giard<sup>86, 8</sup>, E. Gjerløw<sup>54</sup>, J. González-Nuevo<sup>16, 56</sup>, K. M. Górski<sup>58, 91</sup>, A. Gregorio<sup>29, 40, 47</sup>, A. Gruppuso<sup>41</sup>, J. E. Gudmundsson<sup>84, 75, 22</sup>, F. K. Hansen<sup>54</sup>, D. L. Harrison<sup>53, 60</sup>, C. Hernández-Monteagudo<sup>10, 69</sup>, D. Herranz<sup>56</sup>, S. R. Hildebrandt<sup>58, 9</sup>, M. Hobson<sup>4</sup>, A. Hornstrup<sup>13</sup>, G. Hurier<sup>51</sup>, A. H. Jaffe<sup>49</sup>, T. R. Jaffe<sup>86, 8\*</sup>, W. C. Jones<sup>22</sup>, M. Juvela<sup>21</sup>, E. Keihänen<sup>21</sup>, R. Kesitalo<sup>11</sup>, T. S. Kisner<sup>68</sup>, J. Knoche<sup>69</sup>, M. Kunz<sup>14, 51, 2</sup>, H. Kurki-Suonio<sup>21, 37</sup>, J.-M. Lamarre<sup>63</sup>, A. Lasenby<sup>4, 60</sup>, M. Lattanzi<sup>26, 44</sup>, C. R. Lawrence<sup>58</sup>, J. P. Leahy<sup>59</sup>, R. Leonardi<sup>6</sup>, F. Levrier<sup>63</sup>, M. Liguori<sup>25, 57</sup>, P. B. Lilje<sup>54</sup>, M. Linden-Vørnle<sup>13</sup>, M. López-Cañiegos<sup>33, 56</sup>, P. M. Lubin<sup>23</sup>, J. F. Macías-Pérez<sup>66</sup>, G. Maggio<sup>40</sup>, D. Maino<sup>28, 42</sup>, N. Mandolesi<sup>41, 26</sup>, A. Mangilli<sup>51, 62</sup>, M. Maris<sup>40</sup>, P. G. Martin<sup>7</sup>, E. Martínez-González<sup>56</sup>, S. Masi<sup>27</sup>, S. Matarrese<sup>25, 57, 35</sup>, A. Melchiorri<sup>27, 45</sup>, A. Mennella<sup>28, 42</sup>, M. Migliaccio<sup>53, 60</sup>, M.-A. Miville-Deschênes<sup>51, 7</sup>, A. Moneti<sup>52</sup>, L. Montier<sup>86, 8</sup>, G. Morgante<sup>41</sup>, D. Munshi<sup>78</sup>, J. A. Murphy<sup>71</sup>, P. Naselsky<sup>74, 32</sup>, F. Nati<sup>22</sup>, P. Natoli<sup>26, 3, 44</sup>, H. U. Nørgaard-Nielsen<sup>13</sup>, N. Oppermann<sup>7</sup>, E. Orlando<sup>90</sup>, L. Pagano<sup>27, 45</sup>, F. Pajot<sup>51</sup>, R. Paladini<sup>50</sup>, D. Paoletti<sup>41, 43</sup>, F. Pasian<sup>40</sup>, L. Perotto<sup>66</sup>, V. Pettorino<sup>36</sup>, F. Piacentini<sup>27</sup>, M. Piat<sup>1</sup>, E. Pierpaoli<sup>19</sup>, S. Plaszczynski<sup>62</sup>, E. Pointecouteau<sup>86, 8</sup>, G. Polenta<sup>3, 39</sup>, N. Ponthieu<sup>51, 48</sup>, G. W. Pratt<sup>64</sup>, S. Prunet<sup>52, 85</sup>, J.-L. Puget<sup>51</sup>, J. P. Rachen<sup>17, 69</sup>, M. Reinecke<sup>69</sup>, M. Remazeilles<sup>59, 51, 1</sup>, C. Renault<sup>66</sup>, A. Renzi<sup>30, 46</sup>, I. Ristorcelli<sup>86, 8</sup>, G. Rocha<sup>58, 9</sup>, M. Rossetti<sup>28, 42</sup>, G. Roudier<sup>1, 63, 58</sup>, J. A. Rubiño-Martín<sup>55, 15</sup>, B. Rusholme<sup>50</sup>, M. Sandri<sup>41</sup>, D. Santos<sup>66</sup>, M. Savelainen<sup>21, 37</sup>, D. Scott<sup>18</sup>, L. D. Spencer<sup>78</sup>, V. Stolyarov<sup>4, 82, 61</sup>, R. Stompor<sup>1</sup>, A. W. Strong<sup>70</sup>, R. Sudiwala<sup>78</sup>, R. Sunyaev<sup>69, 80</sup>, A.-S. Suur-Uski<sup>21, 37</sup>, J.-F. Sygnet<sup>52</sup>, J. A. Tauber<sup>34</sup>, L. Terenzi<sup>77, 41</sup>, L. Toffolatti<sup>16, 56, 41</sup>, M. Tomasi<sup>28, 42</sup>, M. Tristram<sup>62</sup>, M. Tucci<sup>14</sup>, L. Valenziano<sup>41</sup>, J. Valiviita<sup>21, 37</sup>, F. Van Tent<sup>67</sup>, P. Vielva<sup>56</sup>, F. Villa<sup>41</sup>, L. A. Wade<sup>58</sup>, B. D. Wandelt<sup>52, 85, 24</sup>, I. K. Wehus<sup>58, 54</sup>, D. Yvon<sup>12</sup>, A. Zacchei<sup>40</sup>, and A. Zonca<sup>23</sup>

(Affiliations can be found after the references)

May 19, 2016

## ABSTRACT

Recent models for the large-scale Galactic magnetic fields in the literature have been largely constrained by synchrotron emission and Faraday rotation measures. We use three different but representative models to compare their predicted polarized synchrotron and dust emission with that measured by the *Planck* satellite. We first update these models to match the *Planck* synchrotron products using a common model for the cosmic-ray leptons. We discuss the impact on this analysis of the ongoing problems of component separation in the *Planck* microwave bands and of the uncertain cosmic-ray spectrum. In particular, the inferred degree of ordering in the magnetic fields is sensitive to these systematic uncertainties, and we further show the importance of considering the expected variations in the observables in addition to their mean morphology. We then compare the resulting simulated emission to the observed dust polarization and find that the dust predictions do not match the morphology in the *Planck* data but underpredict the dust polarization away from the plane. We modify one of the models to roughly match both observables at high latitudes by increasing the field ordering in the thin disc near the observer. Though this specific analysis is dependent on the component separation issues, we present the improved model as a proof of concept for how these studies can be advanced in future using complementary information from ongoing and planned observational projects.

**Key words.** ISM: general – ISM: magnetic fields – Polarization

## 1. Introduction

The Galactic magnetic field is an important but ill-constrained component of the interstellar medium (ISM) that plays a role in a variety of astrophysical processes, such as molecular cloud collapse, star formation, and cosmic-ray propagation. Our knowledge of the structure of the mag-

netic fields in our own Milky Way Galaxy is limited by the difficulty interpreting indirect observational data and by our position within the disc of the Galaxy. We know that there are both coherent and random components of the magnetic fields and that in external galaxies they tend to have a spiral structure similar to that of the gas and stellar population (see Beck 2015 for a review). We do not, however, have an accurate view of the morphology of these

\* Corresponding author: T. R. Jaffe,  
tjaffe@irap.omp.eu

field components within either the disc or the halo of our own Galaxy. For a review, see [Haverkorn \(2014\)](#).

There are many modelling analyses in the literature for the large-scale Galactic magnetic fields, including work such as [Stanev \(1997\)](#), [Prouza & Šmída \(2003\)](#), [Han et al. \(2006\)](#), [Page et al. \(2007\)](#), [Sun & Reich \(2010\)](#), hereafter Sun10), [Ruiz-Granados et al. \(2010\)](#), [Fauvet et al. \(2012\)](#), hereafter Fauvet12), [Jansson & Farrar \(2012b\)](#), hereafter Jansson12), [Jaffe et al. \(2013\)](#), hereafter Jaffe13), and [Orlando & Strong \(2013\)](#), hereafter Orlando13). These studies have constrained properties of the large-scale Galactic magnetic fields using complementary observables that probe the magnetic fields in different ways. Most of the constraints so far have come from synchrotron emission, both total and polarized, and Faraday rotation measures (RMs). Thermal dust emission is a useful complement for its different dependence on the field strength and its different source particle distribution. [Fauvet et al. \(2011\)](#) performed the first such joint analysis making use of existing thermal dust polarization data from the ARCHEOPS balloon experiment. Jaffe13 continued with an analysis using Wilkinson Microwave Anisotropy Probe (WMAP) dust polarization instead. Both of these data sets, however, suffer from low signal to noise or limited sky coverage.

The *Planck*<sup>1</sup> data provide a new opportunity to constrain the magnetic fields using the most sensitive full-sky maps to date of both total and polarized dust emission in the sub-mm bands as well as an alternative synchrotron probe in the low frequency bands. Our aim is therefore to add the information from the *Planck* full-sky polarized dust emission maps to our magnetic field modelling and to use their complementary geometry to better constrain the properties of the magnetic fields.

The preliminary work by Jaffe13 in the Galactic plane suggests that constructing a single global model of the Galactic magnetic fields that reproduces both the polarized synchrotron and dust emission over the full sky will be difficult. In this work, we make a first attempt by taking several models in the literature that have been constrained largely by the synchrotron emission and RMs and comparing the corresponding dust prediction to the *Planck* data. Such simple comparisons of the morphology of the resulting polarization sky maps will give insight into how the models can be improved.

Using the comparison of the data to the model predictions for both synchrotron and dust emission, we will perform simple updates to the models where the morphologies do not match and where we can study the physical parameters such as the scale heights and scale radii of the different ISM components. Although constructing new analytic forms is beyond the scope of this work, our analysis will point the way to how we can improve the large-scale field modelling and progress towards a global model that can reproduce all observables.

We will also discuss the difficulties with these analyses, particularly the problem of component separation and the uncertainty in the synchrotron spectral variations over the

sky. The models we present here are based on *Planck* component separation products, and we discuss the limitations of these products and therefore of the resulting models. We will also discuss information from other observables and how the situation will improve in the future based on ongoing and next-generation surveys.

In Sect. 2 we review the data and methods used, referring to appendices for discussion of the *Planck* polarization systematics and component separation issues. In Sect. 3, we describe the synchrotron modelling that, along with RM studies, has led to the development of the magnetic field models we use from the literature. We discuss how they were constructed, on what cosmic-ray lepton (CRL) model they depend, how they compare to each other, and how they need to be updated. In Sect. 4, we present the comparison of the updated models with the *Planck* data for dust polarization and discuss the implications. Lastly, in Sect. 5, we discuss how we expect this work to be improved in the future.

## 2. Data and methods

### 2.1. Observations

#### 2.1.1. *Planck* data

The results presented in this paper are based on the 2015 data release<sup>2</sup> described in [Planck Collaboration I \(2016\)](#), [Planck Collaboration II \(2016\)](#), and [Planck Collaboration VIII \(2016\)](#) including both intensity and polarization results. Because of the presence of numerous astrophysical components at each frequency, we use the **Commander** component separation estimates of the synchrotron and dust total intensities described in [Planck Collaboration X \(2016\)](#). In the case of dust, the purpose is to remove confusion from an intensity offset or cosmic infrared background (CIB). For synchrotron, however, this is more complicated, as the low-frequency total intensity includes several different components in addition to synchrotron emission. The importance of this choice is further discussed in Sect. 2.1.3. The products are given as maps in the HEALPix<sup>3</sup> ([Górski et al. 2005](#)) pixelization scheme in units of mK<sub>RJ</sub> (i.e., brightness temperature), and we downgrade<sup>4</sup> these to a low resolution of  $N_{\text{side}} = 16$  for comparison with the models.

These products consist of spatial information at a reference frequency and a prescription for the spectral model, which we combine to generate the correct prediction for synchrotron emission at 30 GHz and for dust emission at 353 GHz as described in Table 4 of [Planck Collaboration X \(2016\)](#).

We also compare to the full-mission maps of the Low Frequency Instrument (LFI, [Planck Collaboration VI 2016](#)) at a frequency of 30 GHz and the High Frequency Instrument (HFI, [Planck Collaboration VIII 2016](#)) at 353 GHz. Those maps are given in K<sub>CMB</sub> units<sup>5</sup> and require a

<sup>2</sup> <http://pla.esac.esa.int/>

<sup>3</sup> <http://healpix.sourceforge.net>

<sup>4</sup> We simply average the high-resolution pixels in each lower-resolution pixel. This is done for each Stokes parameter, which does not take into account the rotation of the polarization reference frame (see, e.g., [Planck Collaboration Int. XIX 2015](#)). This effect is only significant at the highest latitudes, however, and has no impact on our results.

<sup>5</sup> Temperature units referring to the cosmic microwave background (CMB) blackbody spectrum.

<sup>1</sup> *Planck* (<http://www.esa.int/Planck>) is a project of the European Space Agency (ESA) with instruments provided by two scientific consortia funded by ESA member states and led by Principal Investigators from France and Italy, telescope reflectors provided through a collaboration between ESA and a scientific consortium led and funded by Denmark, and additional contributions from NASA (USA).

unit conversion in addition to colour and leakage corrections based on the instrument bandpasses, as described in [Planck Collaboration II \(2016\)](#) and [Planck Collaboration VII \(2016\)](#). We also make use of the other HFI polarization channels as well as several different methods to correct for systematics, as described in [Appendix A](#).

We note that *Planck* products and the results in this paper are expressed in Stokes  $I$ ,  $Q$ , and  $U$  using the same convention followed by HEALPix for the polarization angle (or equivalently, the sign of  $U$ ) rather than the IAU convention.

### 2.1.2. Ancillary data

We compare the *Planck* synchrotron solution to those from the WMAP analysis by [Gold et al. \(2011\)](#). They used two component separation methods, with several versions each, and we will compare with their basic Markov chain Monte Carlo (MCMC) solution.

We also compare to the 408 MHz map of [Haslam et al. \(1982\)](#) reprocessed as described by [Remazeilles et al. \(2014\)](#). For comparison with previous work such as [Jaffe13](#), we subtract the offset determined by [Lawson et al. \(1987\)](#) to account for the extragalactic components. There is an uncertainty in the calibration zero-level of about 3 K for this survey, which will be further discussed in [Appendix B](#). We also subtract the *Planck Commander* free-free estimate from the 408 MHz map, which is still significant along the Galactic plane. The result is then almost identical to the *Commander* synchrotron solution except for a  $1\sigma$  shift in the zero level.

These ancillary data are available on the LAMBDA<sup>6</sup> website. For comparison to the *Planck* component separation products, see [Appendix B](#).

### 2.1.3. Data caveats

Ideally, studies of the Galactic magnetic fields using synchrotron emission would compare the total and polarized emission at the same frequency in order to measure the degree of ordering in the fields. In order to probe the full structure of the Galactic disc, however, we need to study the emission in the mid-plane where there are two complications. At radio frequencies (below roughly 3 GHz), the synchrotron emission is depolarized by Faraday effects. These impose a so-called polarization horizon<sup>7</sup> beyond which all diffuse polarization information is effectively lost due to the Faraday screen of the magnetized and turbulent ISM. In the microwave bands (tens of GHz), where Faraday effects are negligible, the total intensity is dominated along the Galactic plane by free-free and anomalous microwave emission (AME); see, e.g., [Planck Collaboration Int. XXIII \(2015\)](#). These components have steep spectra in the microwave bands, which makes them difficult to separate from the synchrotron emission.

Therefore, there are two options for this sort of study:

- use the radio frequency for total intensity and microwave frequency for polarization, which subjects the analysis to the uncertainty of assuming a spectral behaviour over a large frequency range that magnifies even

a small uncertainty in the spectrum into a large uncertainty in the amplitude and morphology (e.g., [Sun10](#), [Orlando13](#), and [Jaffe13](#));

- or use the microwave frequencies for both, which subjects the analysis to the significant uncertainty of the component separation in the Galactic plane (e.g., [Jansson12](#)).

These issues are also discussed in [Planck Collaboration XXV \(2016\)](#).

We choose to use the *Planck Commander* component separation results, and though this sounds like the second option, it is effectively the first. The *Commander* analysis fits a model for the synchrotron total intensity based on the 408 MHz map as an emission template and assumes a constant synchrotron spectrum across the sky. That spectrum (see [Sect. 3.1](#)) is in turn the result of a model for the large-scale Galactic magnetic field as well as the CRL distribution, and we use the same model for the latter to be as consistent as possible while studying the former. It must be noted, however, that there is an inconsistency in the analysis. Ideally, the component separation should be a part of the astrophysical modelling, but this is not feasible. An iterative approach would be the next best option, and our analysis here can be considered the first iteration.

It is important to recognize that the various models for the large-scale Galactic magnetic fields in the literature have been developed based on different approaches to these issues. In order to compare these models, the different choices made must be considered. We discuss this further and compare the data sets explicitly in [Appendix B](#).

It is also unclear what effect small but nearby (and therefore large angular-scale) structures have on such analyses. Clearly, models of the large-scale fields will not reproduce individual features such as supernova remnants, but these features may bias our model fitting. We discuss some of these features in [Sect. 3.4.3](#), but we cannot reliably quantify how large an effect they may be having without a better understanding of what these features are. Only when looking through the full Galactic disc in the mid-plane, where such features are small compared to the integrated emission, can we be sure that the resulting models are largely unaffected. We also exclude known regions of localized emission or average over large areas of the sky in order to minimize their impact.

## 2.2. The *hammurabi* code

The *hammurabi*<sup>8</sup> ([Waelkens et al. 2009](#)) code simulates synchrotron and dust emission in full Stokes parameters as well as associated observables such as Faraday RM, emission measure, and dispersion measure. It includes analytic forms for the components of the magnetized ISM (magnetic fields, thermal electrons, CRLs, etc.) or can be given an external file that specifies those components over a spatial grid.

The Sun10 and Fauvet12 magnetic field models are implemented in the publicly available version of *hammurabi*, while the Jaffe13 and Jansson12 models will be included in the next release.

We model the random field component using a Gaussian random field (GRF) simulation characterized by a power-law power spectrum and an outer scale of turbulence. In

<sup>8</sup> <http://sourceforge.net/projects/hammurabicode/>

<sup>6</sup> <http://lambda.gsfc.nasa.gov/>

<sup>7</sup> The distance is dependent on the frequency and the telescope beam but typically of order a few kpc for radio surveys; see, e.g., [Uyaniker et al. \(2003\)](#).



order to compute this component with the highest possible resolution, we split the integration into two steps: firstly from the observer out to a heliocentric distance of  $R < 2$  kpc, and then for  $R > 2$  kpc. For the latter, we simulate the full Galaxy in a 40 kpc by 40 kpc by 8 kpc grid of 1024 by 1024 by 256 bins, i.e., with a resolution of roughly 40 pc. For the  $R < 2$  kpc case, we compute the GRF in a cube 4 kpc and 1024 bins on a side, giving a resolution of 4 pc. We have in both cases run tests with a resolution a factor of two higher in each dimension (requiring several tens of GB of memory) and found the result to be qualitatively unaffected by the resolution. The high-resolution, local part of the simulation has a Kolmogorov-like power spectrum,  $P(k) \propto k^{-5/3}$ , and in both cases we use an outer scale of turbulence of 100 pc (see [Haverkorn & Spangler 2013](#) and reference therein). While the nearby simulation samples different scales, the resolution of the full-Galaxy simulation is too low to be more than effectively single-scale. The ensemble average emission maps are not sensitive to these parameters of the turbulence (though the predicted uncertainty can be, as discussed in Sect. 3.4.1). In both regimes, the GRF is normalized to have the same total rms variation (configurable as shown in Appendix C). This GRF is then rescaled as a function of position in the Galaxy depending on the model (e.g., with an exponential profile in Galacto-centric  $r$  or  $z$ ).

The HEALPix-based integration grid is done at an observed resolution of  $N_{\text{side}} = 64$ , i.e., roughly  $1^\circ$  pixels. As described by [Waelkens et al. \(2009\)](#), the integration grid is refined successively along the line of sight (LOS) to maintain a roughly constant integration bin size. We set the integration resolution parameters to match the resolution of the Cartesian grid for the GRF.<sup>9</sup>

In the case of synchrotron emission, we have explicitly compared the results of a set of GRF simulations with the results from the analytic method used in [Jansson12](#) and verified that the ensemble average is the same. For the dust, we have no analytic expression for the expected emission, so we use the numerical method of GRF realizations for all of the main results of this paper. We compute 10 independent realizations of each model and compare the mean in each pixel to the data in that pixel. We use the variation among the realizations in each pixel as the uncertainty due to the galactic variance, as discussed in Sect. 3.4.1.

### 2.3. Parameter exploration

Though ideally we would perform a complete search over the full parameter space to determine the best values of all parameters, this is computationally not feasible. Such searches have been performed in the past by, e.g., [Jaffe et al. \(2010\)](#) and [Jansson & Farrar \(2012a\)](#). In the first case, the number of parameters was limited and the analysis re-

<sup>9</sup> `hammurabi` uses a configurable number of shells defined by  $N_{\text{shells}}$ . For each shell, its HEALPix  $N_{\text{side}}$  defines a constant angular width for each bin, while an independent variable controls the bin length along the LOS in  $\Delta R$ . The length is constant along the entire LOS, but the width then varies within each shell (see Fig. A.1 of [Waelkens et al. 2009](#).) For the  $R < 2$  kpc integration, we use  $\Delta R = 2$  pc and  $N_{\text{shells}} = 4$ , so that at the last shell the  $N_{\text{side}} = 512$  pixels range from 2 to 4 pc wide from the front to the back of the shell. For the  $R > 2$  kpc integration, we use  $\Delta R = 32$  pc and  $N_{\text{shells}} = 5$ , so that at the last shell the  $N_{\text{side}} = 1024$  pixels range from 16 to 32 pc wide.

stricted to the plane. The full 3D optimization is far more difficult, even excluding the dust emission. In the second case, the fit was performed by using an analytic expression for the synchrotron emission from the random field components, which allows for a very fast computation but does not correctly take into account the variations produced by the modelled random fields. Furthermore, this analytic approach is not possible for dust emission, as there is no correspondingly simple closed-form expression for the ensemble average. (The synchrotron case requires assuming the dependence of the emissivity on  $B^2$ , or equivalently that the CRL spectrum is a power law,  $N(E) \propto E^{-p}$ , with index  $p = 3$ .)

Therefore, the updated models discussed in this paper are only approximations arrived at by visual comparison, focusing on the longitude profiles along the plane and the latitude profile in the inner two quadrants, where the data represent the integration through most of the Galaxy. We accept that in the outer Galaxy away from the plane, the models may not match observations well, but this region represents much less of the Galaxy. We vary key parameters such as the degree of ordering in the fields, the relative strengths of disc and halo components, the scale heights and scale radii of these components, and individual arm amplitudes that affect the emission on large scales. The changes are motivated by the data, but this is subjective rather than quantitative. A complete parameter optimization remains a significant computation challenge for future work.

## 3. Synchrotron modelling

From an observational point of view, the magnetic field can be considered as having three components that contribute to observables differently depending on the sensitivity to orientation and/or direction. (See fig. 1 in [Jaffe et al. 2010](#).) The coherent component (e.g., an axisymmetric spiral) contributes to all observables, since by definition, it always adds coherently. The isotropic random component contributes only to the average total intensity, which co-adds without dependence on orientation; to polarization and RM, it does not contribute to the ensemble average but only to the ensemble variance. A third component, which we call an “ordered” random component following [Jaffe et al. \(2010\)](#) but which was called “striated” by [Jansson & Farrar \(2012a\)](#), contributes to polarization, which is sensitive to orientation, but not to RM, which is additionally sensitive to direction. This third component represents the anisotropy in the random fields thought to arise due to differential rotation and/or compression of the turbulence in the spiral arms of the Galaxy. (See, e.g., [Brown & Taylor 2001](#) or [Beck 2015](#).) These components can only be separated unambiguously using a combination of complementary observables.<sup>10</sup>

The large-scale magnetic field models in the literature are most commonly constrained for the coherent field component. The random field component is not treated specifically in some of these models, nor is the anisotropy in this component often considered, though it has been shown by,

<sup>10</sup> The literature often refers to “random” and “regular” fields, which means that the third component is “random” in the case of RM observations but is “regular” in the case of polarized emission. We prefer to avoid the ambiguous use of the word “regular”.

e.g., Jaffe et al. (2010), Jansson & Farrar (2012a), and Orlando13 to be comparable in strength. Depending on the scientific aims, the random components may either be treated as noise or must be modelled for unambiguous interpretation of the field strengths.

In addition to the model for the magnetic field, we also require a model for the CRLs that produce the synchrotron emission. The following sub-sections describe these elements of the modelling and how changes in each affect the results.

### 3.1. Cosmic-ray leptons

For the synchrotron computation, we require both the spatial and spectral distribution of CRLs<sup>11</sup>. The topic of cosmic ray (CR) acceleration and propagation is a complicated one (see, e.g., Grenier et al. 2015), and there are degeneracies in the space of CR injection and propagation parameters, which can approximately reproduce the synchrotron or  $\gamma$ -ray data that are the primary probes of the particle distributions. It is not the purpose of this work to constrain the particle distributions, so we choose a representative model for the CRLs and discuss how some of our conclusions are subject to the uncertainties in this input. For a further discussion of this topic and in particular the impact on the observed synchrotron emission, see Orlando13.

For this work, we use a model of the CRL distribution as published in Orlando13 and generated using the GALPROP<sup>12,13</sup> CR propagation code. This takes as input the spatial and spectral distributions of the injected primary particles and the magnetic field. It then models the propagation of CRs accounting for energy losses, reacceleration processes, and generation of secondary particles, including positrons. In addition to the primary electrons, our GALPROP model also includes protons and helium in the propagation in order to properly account for the production of secondary leptons.<sup>14</sup>

#### 3.1.1. CRL spatial distributions

The Sun10 analysis used a simple exponential disc distribution. Jansson12 used (A. Strong, D. Khurana, private communications) the spatial distribution of CRLs from a slightly modified version of the “71Xvarh7S” GALPROP model discussed in, e.g., Abdo et al. (2010). The Jaffe13 model was based on the “z04LMPDS” GALPROP model of Strong et al. (2010). For reference, the spatial distributions of these different CRL models (computed with a com-

mon magnetic field model, the Jansson12) are compared in Fig. 1.

#### 3.1.2. CRL energy spectrum

Previous works such as Sun10 and Jaffe et al. (2010) used power-law spectra of a fixed index ( $N(E) \propto E^{-p}$ , where  $p = 3$ ). This is a reasonable approximation above frequencies of a few GeV and was arguably sufficient for early studies of the field morphologies at the largest scales, but it is now insufficiently accurate for the increasing amounts of data available, as demonstrated by Jaffe et al. (2011) and Strong et al. (2011).

For updating the magnetic field models to match the *Planck Commander* synchrotron maps, we use the “z10LMPD\_SUNfE” GALPROP CRL distribution, as derived in Orlando13. This distribution is the latest result of a long-running project including Strong et al. (2010), Strong et al. (2011), and Orlando13 to develop a model for the spatial and spectral distribution of CRLs. In particular, Orlando13 used synchrotron observations and updated not only the CRL scale height but also the turbulent and coherent magnetic field parameters. Various existing magnetic field models were investigated with synchrotron observations, in both temperature and polarization, in the context of CR source and propagation models. The lepton spectrum was adjusted by Strong et al. (2011) to fit the *Fermi* electron and positron direct measurements (Ackermann et al. 2010), while the spatial distribution was the one found to better reproduce the Galactic latitude and longitude profiles of synchrotron emission, after fitting the intensities of the random (isotropic and ordered) and coherent magnetic field components (based on Sun10 for their best fit) to WMAP synchrotron and 408 MHz maps. (We note that this analysis remains subject to degeneracies in the parameter space, in particular at the  $E \lesssim 10$  GeV region of the CRL spectrum where the direct measurements of CRLs are affected by solar modulation.) Because the original name reflects the *resulting* CRLs using the Sun10 magnetic field model, while we of course explore different field models, we will refer to the model for the injected CRs simply as “z10LMPDE”.

This is the base model for the synchrotron spectral template used in the *Planck Commander* analysis, which assumed a constant spectrum derived from this CRL model and fitted only a shift in frequency space (Planck Collaboration X 2016). We choose this CRL model to be as consistent as possible with the component separation, but it is not exactly consistent, since the component separation analysis chose a single synchrotron spectrum to be representative of the sky away from the Galactic plane (see Fig. 2) and allowed it to shift in frequency space in a full-sky analysis.<sup>15</sup> Here, we use the full spatial and spectral distribution produced by GALPROP, varying the magnetic field but keeping the same CR injection model. This is discussed further in Sect. 3.4.2.

Figure 2 compares several synchrotron spectra. The spectral template used in the *Commander* analysis is shown

<sup>15</sup> The logarithmic shift in frequency space by a factor of  $\alpha = 0.26$  was not given an associated uncertainty in Planck Collaboration X (2016). As noted in that paper, this shift was highly dependent on other parameters and was barely detected as different from unity.

<sup>11</sup> These are mostly electrons but include a non-negligible contribution from positrons. We therefore refer to leptons rather than, as is common, simply electrons.

<sup>12</sup> <http://galprop.stanford.edu>

<sup>13</sup> <http://sourceforge.net/projects/galprop>

<sup>14</sup> There is now firm observational evidence for the existence of primary positrons. For references to the observations and demonstration of their primary nature see, e.g., Gaggero et al. (2014) or Boudaud et al. (2015). The lepton spectrum used in the present work reproduces the total electron plus positron measurements. However, positrons do not become significant compared to the electrons until energies well above 20 GeV, which corresponds to synchrotron frequencies much higher than those we consider here, so the question is not directly relevant to this work.

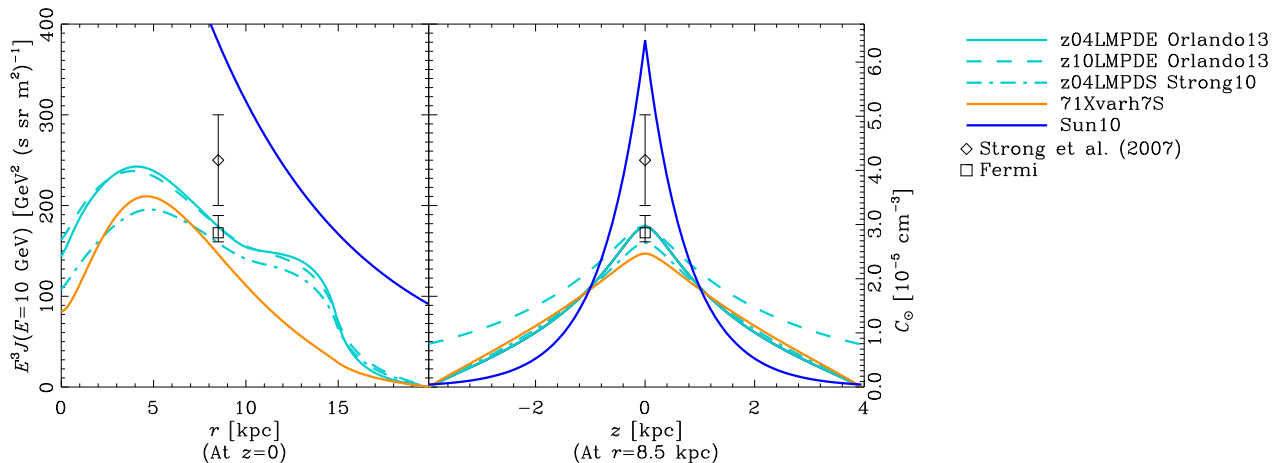


**Fig. 1.** Comparison of CRL distributions. The profile of the CRL density at a reference energy of 10 GeV is shown on the left as a function of Galacto-centric radius for  $z = 0$  and on the right as a function of height at the Solar radius (8.5 kpc). The Sun10 curve does not include the local enhancement described in Sect. 3.2.1. The conversion between the units on the vertical scales at left and right are explained in Jaffe et al. (2010). The *diamond* and *square* symbols show the directly-measured CRL fluxes from Strong et al. (2007) and from Ackermann et al. (2010), respectively. (The former point and its error bar are estimated by eye from their Fig. 4.) The “z04LMPDE Orlando13” and “z10LMPDE Orlando13” models are the more recent versions from Orlando13 for different CRL scale heights of 4 and 10 kpc, respectively, while the “z04LMPDS Strong10” is the older version from Strong et al. (2010). (The z04LMPD model extends to  $|z| = 10$  kpc, though the plot is cut off at  $z = \pm 4$  kpc.)

with and without the spectral shift. This is compared to results computed with *hammurabi* from the same CR source distribution. Since this varies on the sky, an average synchrotron spectrum is computed along the Galactic plane and also for the pixels at  $b = 30^\circ$  for comparison. From these, we compute effective power-law spectral indices,  $\beta$ , from 408 MHz to 30 GHz. The resulting CRL distribution and therefore the synchrotron spectrum depend not only on the injected CRs but also on the magnetic field model assumed through synchrotron losses. The comparison of our results using the z10LMPDE injection model with the  $f(\nu)$  curves is thus approximate. (We compared several of the field models with these injection parameters and found the resulting synchrotron spectra to vary around  $\beta = -3 \pm 0.05$ . The plotted curve is based on the Jansson12 model.)

We see that the single spectral template used in the *Commander* method has a steep spectrum, with a net  $\beta = -3.1$ . The spectral template without the shift is fractionally harder,  $\beta = -3.06$ . The z10LMPDE spectrum (with the same CR injection parameters as underlies the  $f(\nu)$  template but now including the spatial variations) predicts a steeper spectrum at  $b = 30^\circ$  than on the plane. See also Fig. 14 in Planck Collaboration XXV (2016). Also shown for comparison is the CRL model used in the Jaffe13 model, the older z04LMPDS model, which has an effective index that is hardest at  $\beta \approx -2.84$  (which is due to the harder intermediate-energy CR injection spectrum; see Table C.3).

When comparing the effective spectral indices,  $\beta$ , in Fig. 2, note that a difference in the effective spectrum of  $\Delta\beta = 0.04$  (e.g., from the shift in the *Commander* template) corresponds to a difference in the synchrotron intensity extrapolated from 408 MHz to 30 GHz of roughly 20%. A difference of  $\Delta\beta = 0.1$  corresponds to an intensity difference of roughly 50%. These numbers illustrate the uncertainty in the resulting analysis in the Galactic plane based on the uncertainty in the CRL spectrum in the plane, which is closely related to the issue of component separation.

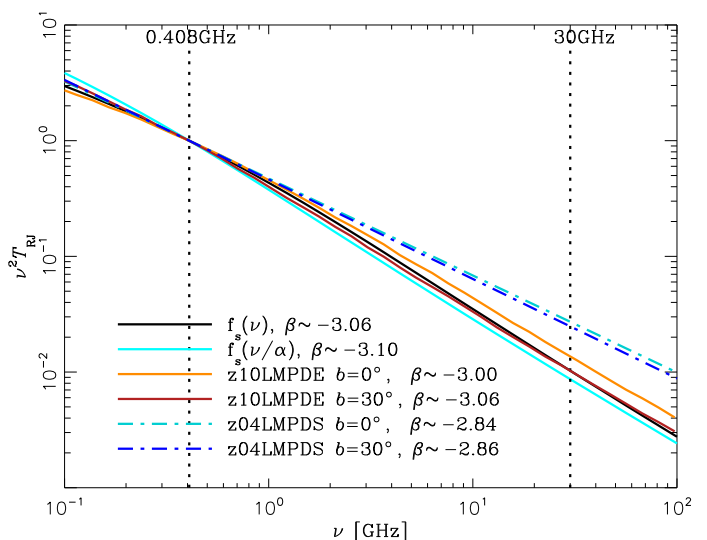


**Fig. 2.** Comparison of synchrotron spectra for different CRL models, all normalized to one at 408 MHz. The black solid curve shows the original spectral template used in the *Commander* analysis, while the cyan solid curve shows the shifted template as described in Planck Collaboration X (2016). In orange is the resulting SED on the plane for synchrotron emission computed using the z10LMPDE CRL model on which the *Commander* template is based. This curve shows the average curve for the Galactic plane, while the brick red is the average for the pixels on a ring at  $b = 30^\circ$ . For these spectra, the effective spectral index  $\beta = \log(A_{30}/A_{0.408})/\log(30/0.408)$  is computed. Lastly, the light and dark blue dot-dashed lines show the power law with the effective indices for the z04LMPDS model averaged at the two latitudes.

In what follows, we will consider the possible extremes and see what statements about the magnetic fields are robust despite this uncertainty.



### 3.2. Magnetic field models from the literature

We choose three models of the large-scale Galactic magnetic field in the literature to be compared with the *Planck* data (LFI and HFI): the Sun10, Jansson12, and Jaffe13 models. This is not meant to be a comprehensive review of the literature. A variety of models have been published, though most tend to be morphologically similar to one of these three. The models used in Page et al. (2007) and Fauvet et al. (2012), for example, are axisymmetric spirals like the Sun10 model, only without the reversal (because they do not make use of RM information). The models of Stanev (1997) and Prouza & Šmída (2003) include spiral arms, either axi- or bisymmetric, and can be considered special cases similar to the Jaffe13 model. The Jansson12 model is a more generic parametrization that can reproduce the largest-scale features of most of these models.

We review these models here, but we do not compare the precise original models with the *Planck* data but rather update them as described in the next section.<sup>16</sup>

#### 3.2.1. Sun10

The “ASS+RING” model of Sun et al. (2008) and Sun10 is a simple axisymmetric spiral field that is reversed in a Galacto-centric ring and in the inner 5 kpc in order to model the RMs in addition to polarized synchrotron emission. The spatial distributions of both CRL density and coherent field strength are modelled with exponential discs. The CRL spectrum is assumed to be a power law with  $p = 3$ . The CRL density model also includes a local enhancement near the Sun’s position to increase the high-latitude emission. This field model also includes a homogeneous and isotropic random component. The model was adjusted by visual comparison with RM data, 408 MHz total synchrotron intensity, and WMAP polarized synchrotron intensity.

The assumed CRL density normalization in the Sun10 analysis is significantly higher than usually assumed. Figure 1 compares the CRL models, where the normalization at the Galacto-centric radius of the Sun was set to  $C_{\odot} = 6.4 \times 10^{-5} \text{ cm}^{-3}$  (at 10 GeV) for the Sun10 model. It is unclear to what degree local values can be considered typical of the Galactic average, but *Fermi*’s direct measurements from Earth orbit near 10 GeV are roughly  $3 \times 10^{-5} \text{ cm}^{-3}$  (Ackermann et al. 2010). Furthermore, the Sun10 model requires an additional enhancement in the form of a 250 % relative increase in a sphere of radius 1 kpc near the Sun’s position (shifted 560 pc towards longitude 45°). This makes their assumed CRL density even more incompatible with *Fermi*’s direct measurements in Earth orbit.

#### 3.2.2. Jansson12

The Jansson & Farrar (2012a,b) model consists of independently fitted spiral segments in a thin disc (each of

which runs from the inner molecular ring region to the outer Galaxy), a toroidal thick disc (or “halo”), and an x-shaped poloidal halo component. This model was optimized in an MCMC analysis in comparison to the RM data as well as synchrotron total and polarized emission from WMAP. Their analysis includes an analytic treatment of the anisotropic turbulent fields. The average emission from this component (which they call “striated” and we call “ordered random”) is computed by scaling up the contribution from the coherent field component appropriately. For total intensity, the expected average emission from the isotropic random component is computed straightforwardly from the assumption of isotropy. This field was developed using a modified version of a CRL prediction from GALPROP discussed in Sect. 3.1.

One interesting comment made by these authors is to note the importance of what Jaffe et al. (2010) call the “galactic variance” (GV), i.e., the expected variation of the synchrotron emission due to the random magnetic field components. They use the data to estimate this variation and use that estimate as the uncertainty in their fitting, but because they use an analytic treatment of these components, they cannot directly model this variance. This will be further discussed in Sect. 3.4.1.

We note that this model was fitted excluding the plane region from the synchrotron polarization analysis. The disc components of the coherent and ordered random fields were then determined by the RM data, while the synchrotron data constrained only the local and halo components. For the synchrotron total intensity analysis, the plane was included in order to fit the random field components in the disc.

#### 3.2.3. Jaffe13

The Jaffe et al. (2010, 2013) model, fitted only in the Galactic plane, consists of four independent spiral arms and a ring component and was optimized with an MCMC analysis. It includes a numerical treatment of the isotropic and ordered random fields, which are constrained by the combination of RM with total and polarized synchrotron emission. The scale heights had not been constrained before.

This model includes the enhancement of the field strength of all components (coherent, isotropic random, and ordered random) in the spiral arms. The arms lie roughly coincident with those of the thermal electron density model of Cordes & Lazio (2002). (See Jaffe et al. 2010, Figs. 2 and 4 for how these features appear when viewed along the Galactic plane and for the definitions of the spiral arms, respectively.) The ordered random field, representing the anisotropy in the turbulence, is generated by adding a component with the same amplitude as the isotropic random component but with an orientation aligned with the coherent field.

This model was developed using the “z04LMPDS” CRL prediction from GALPROP described in Sect. 3.1. It was fitted in the Galactic plane to the RM data, the 408 MHz synchrotron intensity (corrected for free-free emission as described in Jaffe et al. 2011), and the 23 GHz polarization data. This modelling was self-consistent in the sense that the magnetic field model was first used in the CRL propagation, and then the resulting spatial and spectral distribution of CRLs was used in the synchrotron modelling at the two observed frequencies.

<sup>16</sup> In testing the original models, we found it difficult to reproduce precisely the synchrotron intensity normalization according to the respective papers in the case of the Sun10 and Jansson12 models. This is likely related to the different CRL models used and is degenerate with the uncertain CRL normalization. It does not affect the results of the current work, since we use a more recent CRL model and are interested in these models for their morphology.

Jaffe et al. (2010) find evidence for the need to include the ordered random component in order to fit the three complementary observables, while Sun et al. (2008) do not. This is largely due to different assumptions about the CRL density. The Sun10 model assumes a CRL density in the disc more than twice as high as Jaffe13, which means that the coherent field consistent with the RMs then contributes enough synchrotron emissivity to reproduce all of the polarization signal; this is not the case if one assumes the level of CRLs from the GALPROP-based model that matches the *Fermi* CR data.

### 3.3. Updated magnetic field models

The updated models will be referred to as “Sun10b”, “Jansson12b”, and “Jaffe13b”. They are shown in Fig. 3, which makes clear the morphological differences among the three magnetic field models that cannot yet be distinguished using observables integrated through the entire LOS. We note that such a plot of the original models would look visually quite similar.

Here we detail the changes made to each of the models described above in order to match the *Planck* synchrotron solution at 30 GHz in conjunction with the z10LMPDE CRL model. We focus on the longitude profiles along the plane and the latitude profiles averaged over the inner Galaxy ( $-90^\circ < l < 90^\circ$ ). These changes are summarized in Table C.1. The specific values of all changes were simply chosen to approximately match by eye the profiles in Figs. 4 and 5 and as such have no associated uncertainties, nor do they necessarily represent the unique or best solution.

For all models, the first change is to the degree of field ordering in order to match the different synchrotron total intensity estimates in the microwave bands. This firstly requires a global change in the average amounts of random versus ordered fields but also requires morphological changes, since the different field components each combine differently in total and polarized intensities. We attempt to change the smallest number of parameters that still capture the global morphology approximately, such as scale radii and heights, or which project onto a large part of the sky (e.g., the Perseus arm dominates the outer Galaxy). We leave unchanged most of the parameters that affect the coherent field, since those were optimized compared to the Faraday RM data that remain the best tracer of this component. In some cases, however, changes were needed, but we have checked that the RM morphology remains roughly the same.

#### 3.3.1. Sun10b

This model was previously updated in Orlando13 to be consistent with synchrotron polarization from WMAP and total intensity from the 408 MHz data. Our update here is quite similar to this but not identical. In particular, we use a different morphological form for the random field component in the disc.

The original Sun10 model used a uniform distribution of the random field component over the simulation box and a CRL model sharply peaked at  $z = 0$ . The GALPROP CRL model is not as sharply peaked (see Fig. 1), so the synchrotron distribution within  $|b| \lesssim 10^\circ$  requires a modified random field model. We try an exponential disc propor-

tional to  $\exp(-r/r_0) \text{sech}^2(z/z_0)$  consisting of two components: a narrow disc with  $z_0 = 1$  kpc and a thicker disc with  $z_0 = 3$  kpc. (The height of the thick disc is somewhat but not entirely degenerate with a linear offset in the total intensity.) We find that we can fit well the latitude profile, as shown in Fig. 4, using the two-disc model. The amplitude is slightly higher than that in Orlando13.

We add an ordered random component following Jaffe et al. (2010), Jansson & Farrar (2012a), and Orlando13, each of whom found that this additional component is needed to reproduce the polarized emission with a realistic CRL model. As in Orlando13, we add a component simply proportional to the coherent component using the same approach as in the Jansson12 model. We find a slightly higher amplitude than Orlando13 for this component. These differences reflect the different data sets used and are likely related to the additional spectral shift in the Commander component separation solution.

#### 3.3.2. Jansson12b

As with all models, first the random component amplitude has to change to correct the degree of ordering in the field near the plane. This also matches much better the galactic variance discussed in Sect. 3.4.1. With only this change, the morphology no longer matches well, not only because of the different CRL distribution, but also because the coherent and random fields have different distributions, and the change in their relative strengths changes the morphology of the sum.

With the new CRL distribution, the high-latitude synchrotron polarization is too high. We therefore lower the amplitude of the x-shaped field component. (This is degenerate with other parameters such as the amplitudes of the toroidal halo components.) Along the plane, the polarization is also too strong in the outer Galaxy, so we drop the coherent field amplitude of the Perseus arm (segment number six in Fig. 3 and Table C.1). (This is degenerate with the increased CRL density in the outer Galaxy.)

The results of the parameter optimization in Jansson12 include a set of spiral segments for the random field components that are dominated by a single arm. One arm is more than twice as strong as the next strongest, and in terms of synchrotron emissivity, which goes roughly as  $B^2$ , this is then a factor of 4 higher. In other words, the synchrotron total intensity is dominated by a single spiral arm segment in the Jansson12 model. The quoted uncertainties on their fit parameters do not take into account the systematic uncertainties in the component-separated map that they used for synchrotron total intensity, and we consider these parameters to be unreliable in detail. Because of this and the physically unlikely result of one dominant turbulent arm, we further modify this model to distribute the random component more evenly through alternating spiral arm segments. As discussed by Jaffe13, the distribution of the synchrotron emission in latitude and longitude is not very sensitive to precisely where the disordered fields lie in the disc. (The Jansson12 fit that resulted in one dominant arm segment was likely driven by individual features that may or may not be reliable tracers of large-scale morphology.) The precise *relative* distributions of ordered and disordered fields make a larger difference for the dust, however, and this will be discussed further in Sect. 4.3.



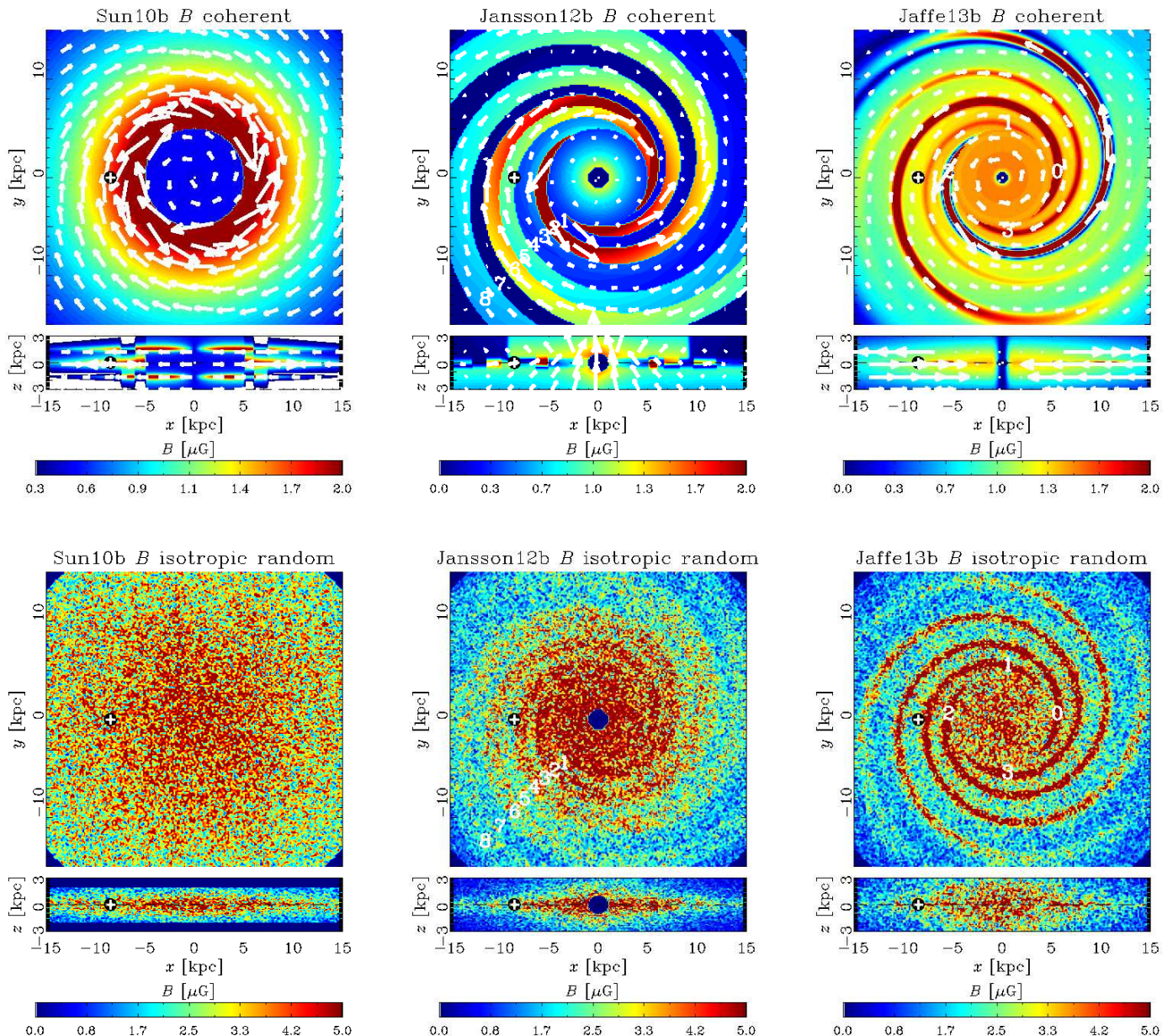


**Fig. 3.** Comparison of the updated magnetic field models described in Sect. 3.3. Each *column* shows one of the models. The top row shows both the coherent field amplitude in colour (on a common scale) and the projected direction shown by the arrows. The top portion of each panel shows the  $x$ - $y$  plane at  $z = 0$ , while the bottom portion shows the  $x$ - $z$  plane at  $y = 0$ . The bottom row shows the amplitude of a single realization of the isotropic random field component. The white cross in a black circle shows the position of the observer.

As discussed above, we replace the analytic estimate for the total synchrotron emission from the isotropic random component with numerical simulations of a GRF. We retain, however, the simple generation of their ordered random component by simply scaling up the coherent component. This means that we are missing the ordered random field’s contribution to the galactic variance.

### 3.3.3. Jaffe13b

For the Jaffe13 model, the different components’ scale heights need to be adjusted, since these had not been constrained by the previous analysis confined to the Galactic

plane. We now use the values listed in Table C.1. To match the synchrotron latitude profiles in total and polarized intensities, we now use two exponential discs, as for Sun10b, one a thin disc and one thick, or “halo”, component for each of the coherent and random field components. We also flip the sign of the axisymmetric components (disc and halo, but not the arms) above the plane to match the RM asymmetry as discussed in Sun et al. (2008).

The combination of a different method for estimating the total synchrotron intensity and the updated CRL model require a corresponding change in the degree of field ordering. We therefore decrease the amplitude of the random component.

Because of the difference in the CRL distribution between the inner and outer Galaxy, we adjust slightly some of the arm amplitudes. The field amplitude in the Scutum arm drops, as it does in the molecular ring.

Lastly, we do not include the shift in the spiral arm pattern introduced in Jaffe13 between the arm ridges of the isotropic random field component and the rest of the components. This shift was introduced to increase the dust polarization and was motivated by observations of external galaxies. As we will see in Sect. 4.2, the updated models produce more strongly polarized dust emission without this additional complexity.

### 3.4. Synchrotron results

Figures 4 and 5 compare the data with the ensemble average models in profiles in longitude and latitude. They demonstrate that each of the three Galactic magnetic field models can be configured to reproduce roughly the right amount of emission in total and polarized intensity towards the inner Galaxy (which covers most of the Galactic disc), despite the significant morphological differences in the field models shown in Fig. 3. They do, of course, differ in detail, including polarization angles not visible in those plots, and they do not fit well in the outer Galaxy. Figure 6 shows maps of the data and models in Stokes  $I$ ,  $Q$ , and  $U$  as well as the differences.

In both profiles and maps, we also plot the residuals as differences divided by the expected galactic variations computed from the models. These variations are model-dependent, since the amplitude of the random field component impacts not only the mean total intensity of synchrotron emission but also the expected variation of our single Galaxy realization from the mean. This means that the significance of the residuals is model-dependent and should be treated carefully. The question of this galactic variance is discussed as an observable in itself in Sect. 3.4.1.

These residuals show clearly the North Polar Spur (NPS) and exclude the Galactic centre region, neither of which is treated explicitly in the modelling. We can see an excess of total intensity emission at high latitudes in the data compared to all models, which may be due to a missing isotropic component in the models or to the uncertain offset level of the 408 MHz map used in the *Commander* synchrotron total intensity solution. In polarization, we see strong residuals in all models in the so-called Fan region in the second quadrant near the plane. In the following sections, we discuss the most important aspects of the synchrotron modelling: the information in the galactic variance and the impact of a varying synchrotron spectrum. We emphasize the dependence of these results on our choice to base the modelling on the *Planck Commander* component-separation products.

#### 3.4.1. Galactic variance

In comparing model predictions with the observables in the presence of a random field component, we must take into account the fact that the observables do not represent the ensemble average galaxy. Instead, they represent one turbulent realization, i.e., our Galaxy, and therefore we do not expect the models to match precisely. The models do, however, predict the degree of variation due to the random

magnetic fields. We refer to this as galactic variance. These predictions are not only necessary for estimating the significance of residuals but also an additional observable in and of themselves.

Jansson & Farrar (2012a) computed their model entirely analytically and therefore obtained no prediction for the galactic variance. They recognize its importance as an observable, but they only estimate this variance from their data to use in their likelihood analysis. For each low-resolution  $N_{\text{side}} = 16$  pixel, they compute the rms variation of the data at its nominal resolution ( $1^\circ$  in the case of WMAP foreground products). We test this approach by comparing with the results of the identical operation on a set of simulated galaxy realizations. Specifically, for each realization, we compute the rms in each large pixel, and then take the average among the realizations. The Sun10 analysis did compute a random component but did not look at this issue. The analyses on which the Jaffe13 model is based did compute such realizations and the resulting variance, and it was used in the model comparison plots and the likelihood computation but not examined as an observable in itself.

Jansson & Farrar (2012a) do not show whether their model for the isotropic random component of the magnetic field in Jansson12 results in a variance similar to what they measure with their  $N_{\text{side}} = 16$  pixel-based variance estimate. Figure 7 shows this comparison explicitly.

The top row of Fig. 7 gives the data rms variation using the method from Jansson & Farrar (2012a,b). From left to right, we show this rms for synchrotron total  $I$  from *Commander*, for Stokes  $Q$  from WMAP MCMC (extrapolated to 30 GHz assuming  $\beta = -3$ ), and Stokes  $Q$  at 30 GHz from LFI. We do not show Stokes  $U$ , which is very similar to  $Q$ .

The second through fourth rows of Fig. 7 show the  $N_{\text{side}} = 16$  rms variations predicted by the three models for comparison with the data. Because the variations in the data include both GV and noise variations, we add to the models in quadrature the expected noise level of LFI computed from the diagonal elements of the published covariance matrix. For comparison with WMAP in the middle column, we add an estimate of the noise level computed from the published  $\sigma_0$  and the  $N_{\text{obs}}$  for the K-band at 23 GHz. For both surveys, the noise has a quite distinct morphology from the GV in the models, with noise minima near the ecliptic poles due to the scan pattern visible similarly in both observed and simulated maps. We include the noise for comparison, but it is the GV that is of interest.

These comparisons of models and data show some significant differences. The original Jansson12 model significantly overpredicts the variation in the synchrotron polarized emission, while the updated model somewhat underpredicts the variation. This implies in each case an incorrect degree of ordering in the fields.

We note, however, that the method using the sky rms has little sensitivity to fluctuations significantly larger than the  $N_{\text{side}} = 16$  pixels, which are roughly  $4^\circ$  wide. If the outer scale of turbulence is roughly 100 pc, then fluctuations on these scales are not fully accounted for when nearer than about 1.5 kpc. In other words, the sky rms method is not representative of the emission variations due to local structures within this distance, but this applies equally to the data and to the models.



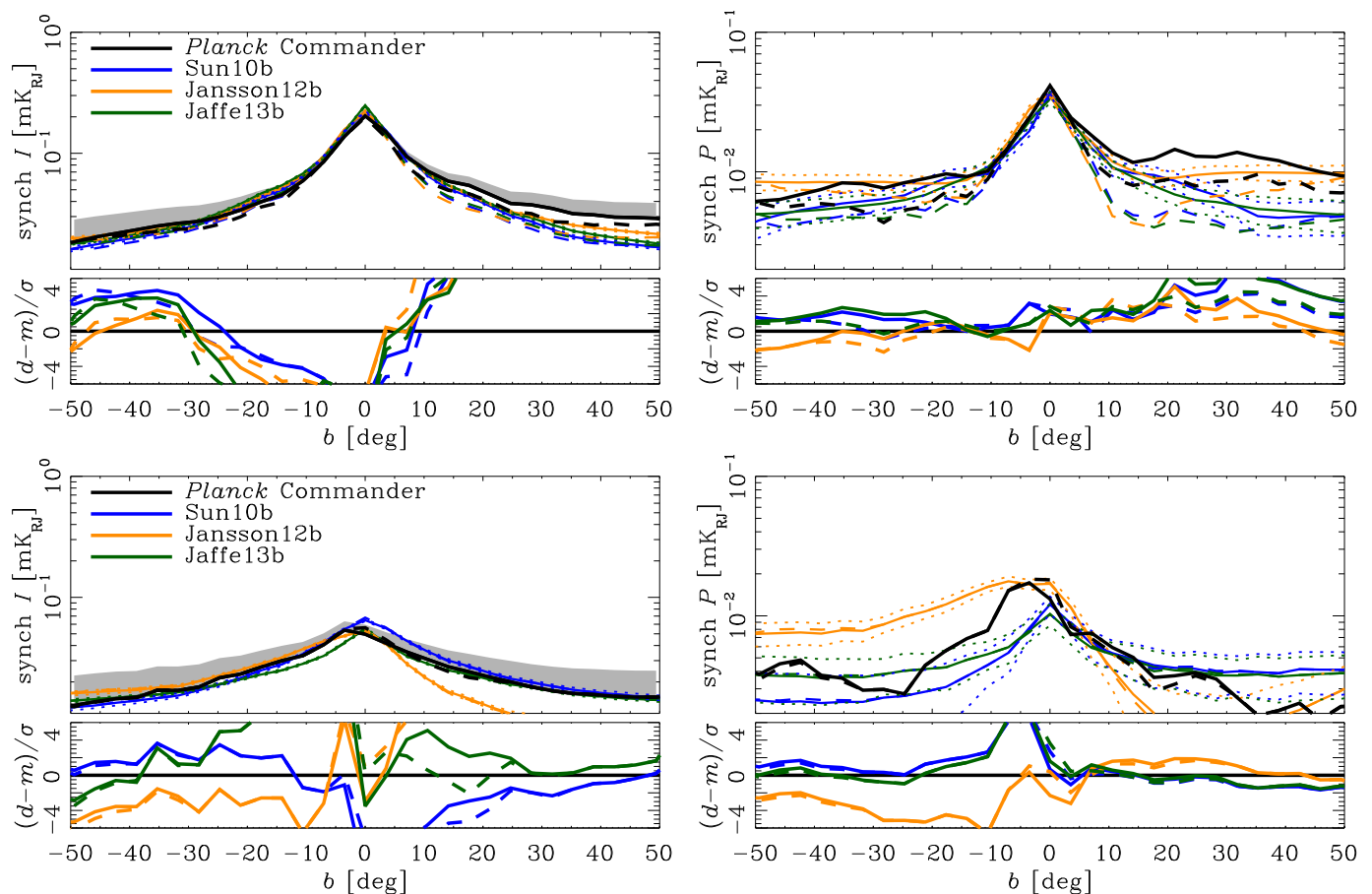


**Fig. 4.** Synchrotron latitude profiles for the data and the updated models' ensemble average. The observables are averaged over a range of longitudes for a given latitude bin, and on the left is total intensity and on the right polarized intensity. The top shows the inner Galaxy (i.e.,  $-90^\circ < l < 90^\circ$ ), while the bottom shows the third quadrant ( $180^\circ < l < 270^\circ$ , i.e., the outer Galaxy excluding the Fan region). The dotted coloured lines show the model mean plus or minus the expected variation predicted by the models (though these are often too close to the solid lines to be visible). This variation is also the  $\sigma$  used to compute the significance of the residuals in the bottom panel of each row. The dashed curves show the profiles excluding the loops and spurs discussed in Sect. 3.4.3. The grey band shows the  $\pm 3$  K zero-level uncertainty of the data at 408 MHz extrapolated with  $\beta = -3.1$ .

The high level of random field in the original Jansson12 model was likely caused by the contamination of the microwave-band total intensity synchrotron observables by anomalous dust emission. The updated model may underpredict the emission because it is too far the other way due to the steep spectral index assumed for the synchrotron spectrum in the *Planck Commander* solution. (In the case of the Sun10b and Jansson12 models, the simulations do not include the variation due to the ordered random component. They are therefore missing some of the expected physical variations. The Jaffe13b model, however, does include this in the simulations and shows a similar degree of variation.)

The Jansson12 analysis uses these estimates of the uncertainty in the  $\chi^2$  computation in their likelihood exploration of the parameter space. Given that the variations are overpredicted in polarization, this could easily allow incorrect models to fit with unrealistically low values of  $\chi^2$  giving the appearance of a good fit.

We also show for comparison on the bottom row of Fig. 7 the actual galactic variance computed for the models by using a set of realizations of each. In this case, we compute the variation *among* the different realizations for each full-resolution pixel and then downgrade (i.e., average) the re-

sult to  $N_{\text{side}} = 16$ . This shows the true galactic variance in the simulations, including the largest angular scales, which is a quantity we cannot compute for reality but which is interesting to compare. It is the uncertainty we use in this work for comparing models to the data, since it expresses how much we expect the real sky to deviate from the model average. Unlike the rms method, the GV method does include local structures as long as they are resolved by the simulation (see Sect. 2.2). On the other hand, the rms measured on the real sky includes variations down to arbitrarily small scales (as long as they are far enough away to be sampled within the size of the  $N_{\text{side}} = 16$  pixel). For the models, this is limited by the resolution of the simulation, and so the model estimates using both rms and GV will always be missing some variations at small spatial scales.

The rms method does, however, predict more variation in the Galactic plane than the GV method does (compare the last two rows on the left of Fig. 7). This is not a simulation resolution issue, since both are based on the same simulations. Instead, this is due to the fact that the Galactic emission components all have steep gradients at low latitudes, and this contributes variance within the large pixel in the rms method that is not due to the turbulent field component. It is therefore impossible to directly compare



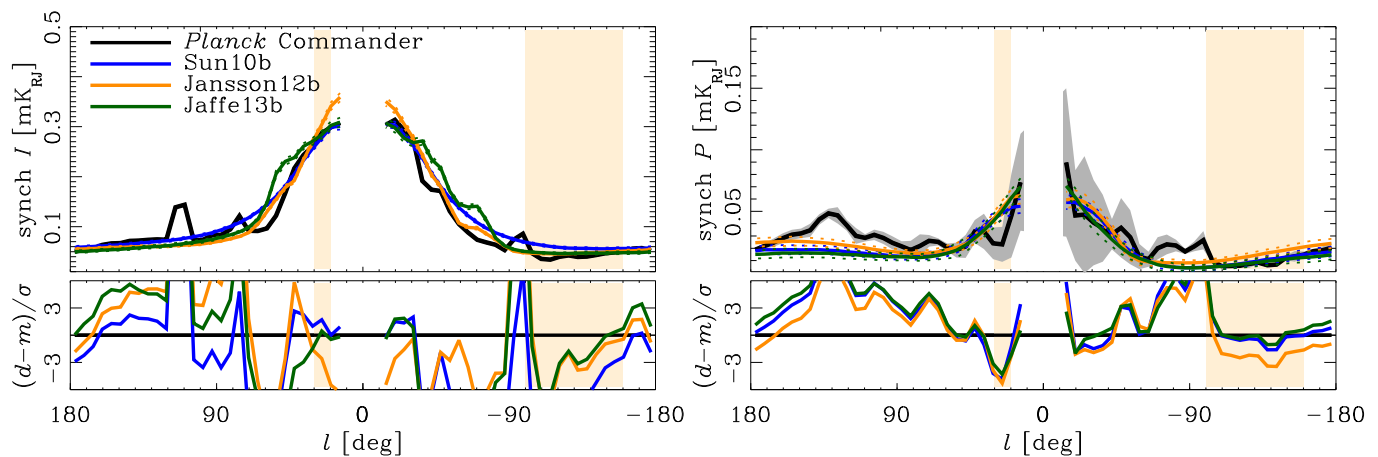


**Fig. 5.** Longitude profiles for synchrotron for the updated models as described in Sect. 3.3. See Fig. 4. The grey band is an estimate of the uncertainty primarily due to bandpass leakage discussed in Appendix A.1. The pale orange vertical bands highlight longitude ranges where the plane crosses any of the loops discussed in Sect. 3.4.3.

the different methods. (This gradient contributes to the rms of both simulations and sky, however, so the comparison of those two remains valid.)

We have also tested the effect of the simulation resolution on these estimates of the GV. We dropped the simulation resolution by a factor of 2 as well as increasing it by a factor of 2. The lowest resolution does significantly affect the analysis, but our chosen resolution is within a few percent of the highest resolution estimate over almost all of the sky, differing by up to 20% in the inner Galactic plane only.

The variance discussed here is related to the strength of the isotropic random magnetic field component relative to the coherent and ordered components, which, as discussed in Sect. 3.3, is related to the estimate for the synchrotron total intensity in the microwave bands. This in turn is a function of the CRL spectrum assumed, which is highly uncertain and varies on the sky. The original Jansson12 model (in the middle column of the fourth row of Fig. 7) shows the hardest spectrum considered, since it is based on the WMAP MCMC solution that effectively assumes  $\beta = -2.6$  in the Galactic plane and therefore has the highest level of random fields and variance. The updated models shown on the right of that figure are tuned to match the *Planck Commander* synchrotron solution that assumes a spectrum with an effective index of  $\beta = -3.1$ . This is at the steep end of reasonable for the sky as a whole and may be too steep for the Galactic plane region. And indeed, the original model overpredicts and the updated model underpredicts the variance in the polarization.

The fact that the updated models appear to underestimate somewhat the variations implies that the residuals computed as  $(d - m)/\sigma$  will appear more significant than they perhaps are. It is important, however, to keep in mind when looking at the residuals how the uncertainties themselves are model-dependent, and therefore so is the significance of any residual. For example, one could make polarization residuals appear less significant by increasing the random component. An explicit likelihood-space exploration should take this into account in the parameter estimation (see, e.g., Eq. 14 of Jaffe et al. 2010 where this was done), but our approximate fitting here does not. (Nor

was this done in the Jansson12 analysis.) This will have to be dealt with correctly in any future analysis with a correct parameter estimation once the component-separation problem has been solved.

Lastly, we note that the modelled GV is also a function of other properties of the random field component such as the outer scale of turbulence and the power-law index. We have tested the effects of varying these parameters as much as possible given the dynamic range in our simulations. A larger turbulence scale results in a larger GV, since the GV is partly a function of the number of turbulent cells in each observed pixel. Likewise, a steeper turbulence spectrum (i.e., more dominated by the largest scales) causes an increase in the GV, though this effect is fairly weak. These effects should be kept in mind when looking at the predicted amount of GV for each model, but the chosen parameters are well motivated by observations of the ISM, as discussed by Haverkorn & Spangler (2013).

### 3.4.2. The synchrotron spectrum

We have adopted in our analysis the *Planck Commander* synchrotron solution, which assumes a constant spectrum on the sky that can shift in frequency space (which effectively steepens or hardens it). The component separation is only sensitive to the effective spectral index between the microwave regime and the 408 MHz total intensity template. This assumed synchrotron spectrum was originally based on an analysis of radio data at intermediate latitudes in Strong et al. (2011). (The Orlando13 follow-up studied the influence of the magnetic field models but did not change the spectral parameters of the injected electrons.)

The resulting *Commander* synchrotron spectrum is quite steep, with an effective  $\beta = -3.1$  from 408 MHz to the microwave bands. This fit is likely driven by the intermediate- and high-latitude sky; near the plane other components (free-free and AME) are strongly correlated, while the higher latitudes are dominated by synchrotron, particularly strongly emitting regions like the NPS. This result should therefore not be taken as evidence for such a steep spectrum of synchrotron emission in the Galactic plane. On the contrary, the use of this spectrum ignores the fact that there

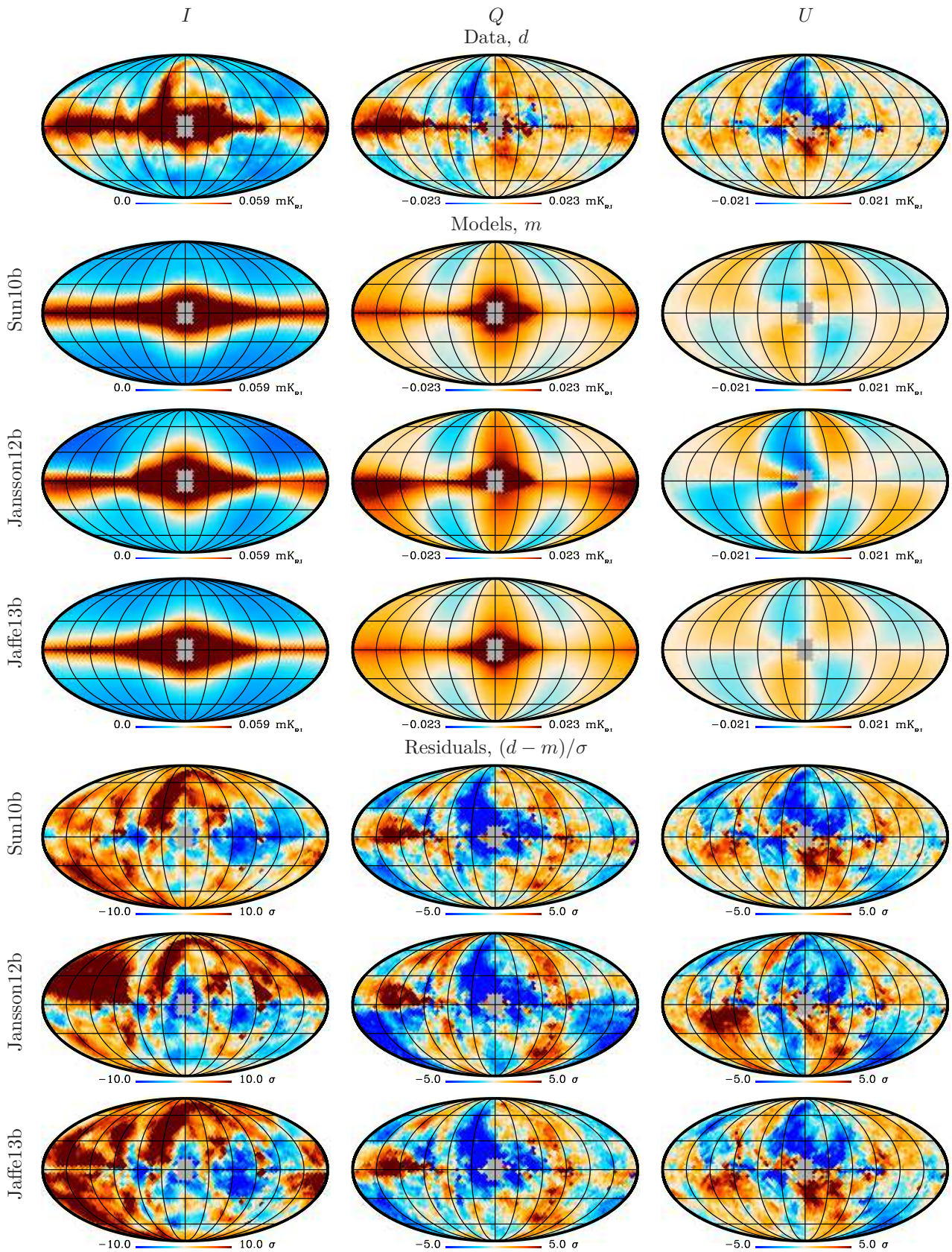


**Fig. 6.** Comparison of the model predictions for synchrotron emission and the *Planck* synchrotron maps. The columns from left to right are for Stokes  $I$ ,  $Q$ , and  $U$ , while the rows are the data followed by the prediction for each model, and lastly the difference between model and data divided by model uncertainty (galactic variance).



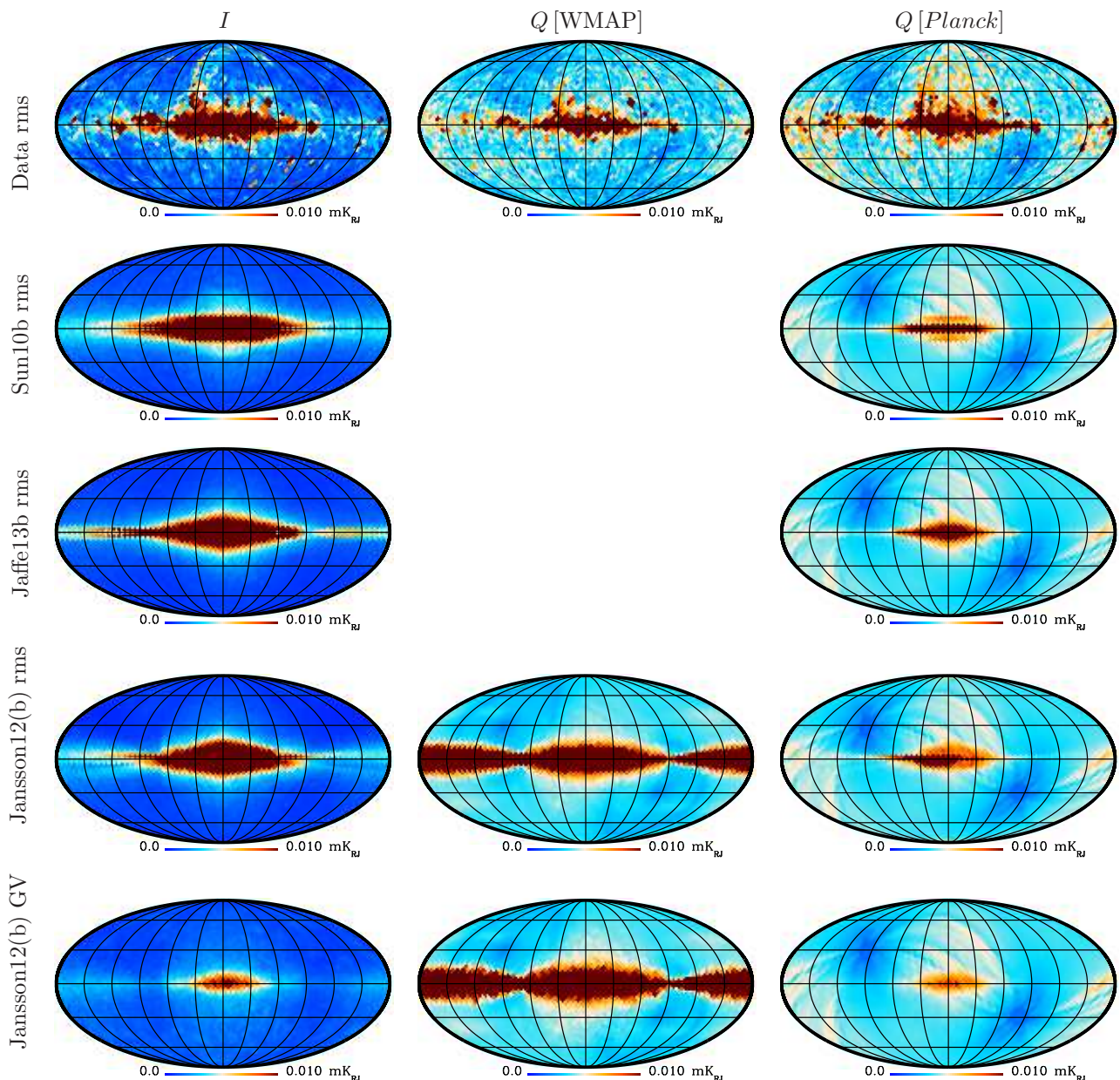


**Fig. 7.** Comparison of estimates for galactic variance in data and models. The top row shows estimates from the data, while the following rows show the model predictions. Excepting the last row, these estimates are based on the rms variations in each low-resolution ( $N_{\text{side}} = 16$ ) pixel. From left to right, the top row shows the estimates from the synchrotron total intensity from **Commander**, the synchrotron  $Q$  map from WMAP MCMC (extrapolated to 30 GHz), and the synchrotron  $Q$  map from **Commander**. (The Stokes  $U$  maps, not shown, look very similar to those for  $Q$ .) The updated Sun10b model is on the second row, the updated Jaffe13b model on the third row, and two versions of the Jansson12 model are in each of the fourth and bottom rows. To each model prediction of the ensemble variance is added simulated noise. In the case of Sun10b and Jaffe13b, we only show the updated model but for Jansson12, we compare the original model (*middle column*) optimized with WMAP MCMC  $I$  and  $Q$  and the updated Jansson12b model (*left and right*) optimized with the **Commander** synchrotron solution. For comparison, the last row shows the full galactic variance in each pixel for the Jansson12 models, as described in the text.

is evidence for a global hardening of the spectrum in the Galactic plane and also for a larger curvature in the spectrum at low frequencies.

There are a variety of studies that find evidence for the steepening of the spectrum with Galactic latitude, such as Fuskeland et al. (2014) and references therein. Their results imply that the spectrum *within* the WMAP bands themselves hardens by  $\Delta\beta = 0.14$  in the plane compared to the rest of the sky. More recently, a similar steepening of about 0.2 in the microwave bands off the plane was found by the

QUIET project (QUIET Collaboration et al. 2015). Both find a steeper index of  $\beta \approx -3.1$  off the plane, consistent with what **Commander** finds, while the index in the plane can be  $\beta \approx -2.98$  (Fuskeland et al. 2014) or as hard as  $\beta \approx -2.9$  in the QUIET data. The steepening seen by Fuskeland et al. (2014) is measured above  $|b| \approx 15^\circ$ , as they analysed the whole sky with a set of large regions. The QUIET analysis, however, found the steepening as close as  $|b| > 2.5^\circ$  from the plane. It is therefore unclear in how narrow a region the microwave spectrum hardens.



Furthermore, evidence for the hardening of the synchrotron spectrum at low frequencies in the plane comes from [Planck Collaboration Int. XXIII \(2015\)](#), which found that the synchrotron emission on the plane has a spectral index in the radio regime of  $\beta = -2.7$  between 408 MHz and 2.3 GHz. This is a separate question to that of the difference between the plane and the higher-latitude sky in the microwave bands. This paper also identifies two distinct synchrotron-emitting regions: a narrow  $|b| \approx 1^\circ$  component and a wider  $2^\circ \leq |b| \leq 4^\circ$ , which they interpret as having different origins. Their hard spectrum applies again to this very narrow region along the plane.

If these two results are correct, i.e., that in the radio regime the spectrum in the plane is  $\beta = -2.7$  and in the microwave regime the spectrum in the plane is  $\beta = -2.9$ , then the total effective spectrum from 408 MHz to 30 GHz is  $\beta \approx -2.8$  depending on exactly where the turnover occurs.

This would imply that the *Planck Commander* synchrotron solution underpredicts the synchrotron total intensity in the plane by nearly a factor of 4.

The  $\beta = -2.6$  hardening in the plane in the WMAP solution, however, may partly be due to contamination by AME and free-free emission. The former is not explicitly included in the WMAP MCMC component separation used by Jansson12.

Figure 8 shows the effective synchrotron spectral index from the models at 30 GHz to the data at 408 MHz. In other words, we compute  $\beta$  from the maps by averaging over the inner Galaxy for each latitude bin and computing

$$\beta = \frac{\ln(m_{30}/d_{0.408})}{\ln(30/0.408)}.$$

The updated models are all around  $\beta \approx -3.1$  with variations where the models do not quite match the morphology of the data, particularly in the north around the NPS.<sup>17</sup> The original Jansson12 model (developed to fit the WMAP MCMC synchrotron) implies a much harder index at low latitudes.

Reality is therefore likely to be somewhere in between the steep spectrum of the *Planck Commander* solution and the hard spectrum of the WMAP MCMC solution. The Galactic magnetic field models, similarly, may be considered as bracketing reality. The original Jansson12 model had too much random magnetic field, while the updates here based on *Planck Commander* results likely have too little. If this is indeed the case, it might explain why our residuals are much larger than the model variance, i.e., the  $(d-m)/\sigma$  plots in Figs. 4 through 6 have a large range; the models may well underestimate the expected variance.

[Fuskeland et al. \(2014\)](#) also find that the synchrotron spectrum is hardest when looking tangentially to the local spiral arm ( $l \approx \pm 90^\circ$ ) of the Galaxy and is steepest towards both the Galactic centre and anti-centre. Such a large variation is not reproduced by the GALPROP model, implying something incorrect in the spatial modelling of the CR injection or propagation. The difference is of order  $\Delta\beta \approx 0.2$ ,

<sup>17</sup> Because we use the full GALPROP CRL spatial distribution, not the single spectral template used in the *Commander* analysis, the models do include a variation of the synchrotron spectral index on the sky of  $\Delta\beta \lesssim 0.05$ . This does not enter into our analysis, which is confined to a single synchrotron frequency, but if one took our resulting model and generated the prediction at 408 MHz, it would differ from the 408 MHz data due to these variations.

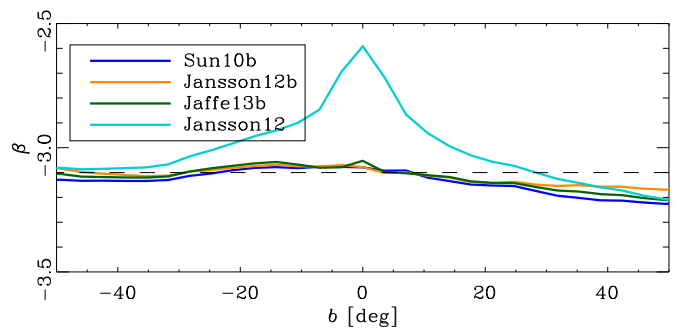


**Fig. 8.** Effective synchrotron spectral index,  $\beta$ , between models at 30 GHz and the data at 408 MHz as averaged over latitude bins in the inner Galaxy ( $-90^\circ \leq l \leq 90^\circ$ ).

and this variation also affects the determination of the average spectrum in the Galactic plane. Taking it into account, the average spectrum could then be as hard as  $-2.85$  with a corresponding impact on the implied synchrotron intensity in the plane.

### 3.4.3. Radio loops and spurs

As pointed out in [Planck Collaboration XXV \(2016\)](#), the inner regions of the Galactic plane show a thickened disc in total intensity that does not have a counterpart in polarization. The latter instead shows only a thin disc and a set of loops and spurs that cross the plane. These loops and spurs are indicated in Fig. 9, along with the outline of the *Fermi* bubbles.

Figure 10 shows a zoom of the inner Galaxy in synchrotron polarized intensity for the data at 30 GHz and for two of the models. The ridges of the spurs and loops as defined in [Planck Collaboration XXV \(2016\)](#) are over-plotted. (See also [Vidal et al. 2015](#).) The thickness of the disc visible in polarized emission between the spurs is clearly narrower in the data than in the models. The latitude profiles in Fig. 4 that show a rough match for the data when averaged over a broad range in longitude are therefore somewhat misleading, as they average over these structures as well. The ordered fields may be distributed in a narrower disc than the current models.

We test the effect of removing the brightest parts of these features by applying the mask shown in Fig. 9. This is a downgraded version of the mask shown in figure 2 of [Vidal et al. \(2015\)](#) and includes a mask for the edges of the *Fermi* bubbles. We show the profiles in latitude when excluding these regions as the dashed lines in Fig. 4. For the longitude profiles, the masking would exclude the regions denoted by the two vertical bands in Fig. 5.

Two regions in the Galactic plane are removed by this mask: the region near  $l \approx 30^\circ$  where the NPS intersects the plane and another from  $-160^\circ \lesssim l \lesssim -110^\circ$ . In the first region, the models overpredict the signal significantly compared to the data. This region may be depolarized due to the fact that the orientation of the polarization in the spur is perpendicular to that of the diffuse emission in the plane, and there is a cancellation along the LOS. In the second region at negative longitudes, the loop is roughly parallel to the plane where it intersects, and so a similar structure should co-add rather than cancel with the diffuse emission, but little effect is seen. The latitude profiles show how much the emission both to the north and south

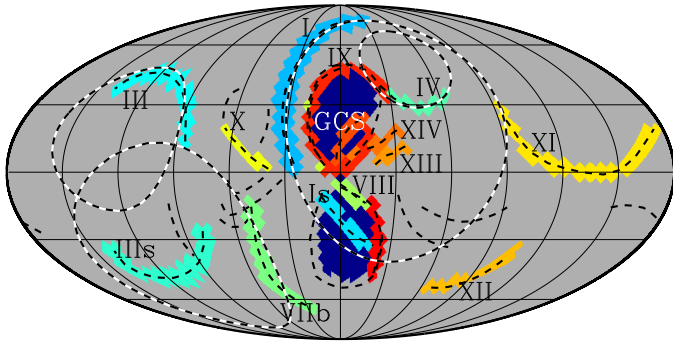


**Fig. 9.** The regions masked for each of the loops and spurs defined by [Planck Collaboration XXV \(2016\)](#) and [Vidal et al. \(2015\)](#) as well as for the region on the edge of (red) or inside of (dark blue) the *Fermi* bubbles. The dashed lines delineate the emission ridges (black) and the four largest radio loops at their original locations (black and white).

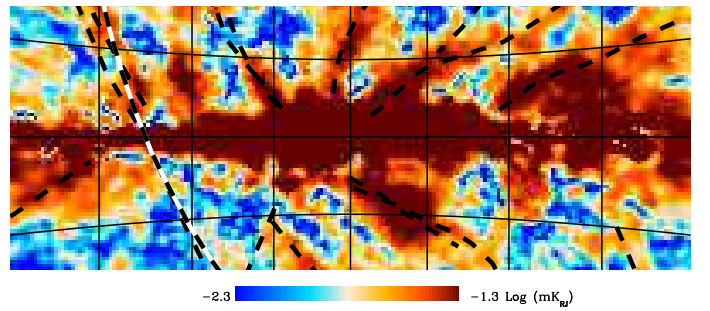
is reduced by the exclusion of the brightest ridges. The significance of the residuals drops, which is unsurprising when we mask out bright and clearly localized regions not reproduced by the models, but the residuals remain higher in the north than the south.

These comparisons show how the presence of the loops and spurs can affect the large-scale modelling by either cancelling or adding polarized emission to the diffuse component. Though we can mask the brightest of these features, the interiors also contain emission that is visibly related to the loop. In the case of the NPS, the interior likely covers a significant fraction of the sky and may have a substantial effect on attempts to fit large-scale magnetic field models.

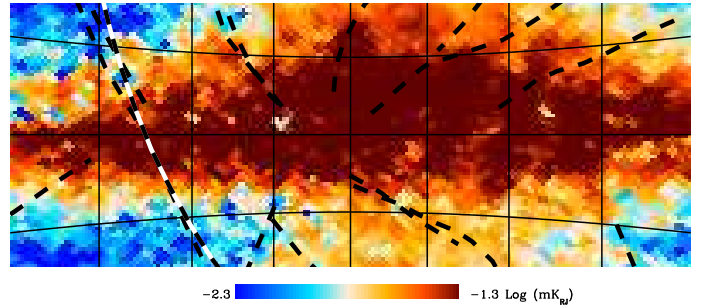
#### 4. Dust modelling

We now take the models whose synchrotron emission we have examined above and look at the predicted dust emission and compare it to the *Planck* observations in total and polarized intensity at 353 GHz.

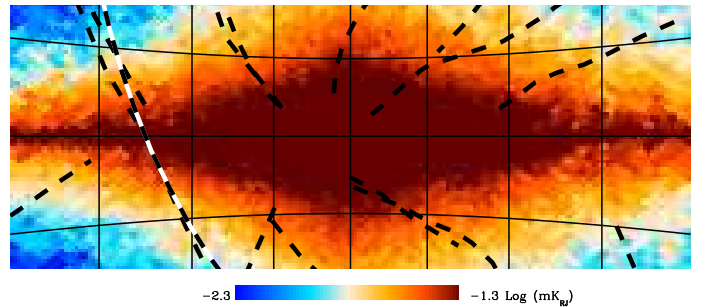
Fauvet12 performed the first fitting of the large-scale field to dust emission. They fitted a magnetic field model to both polarized synchrotron emission and polarized thermal dust emission using the WMAP and ARCHEOPS data, respectively. One important aspect of their analysis is the use of intensity templates to account for localized variations. Fauvet12 used the simple exponential distributions of the magnetized ISM components and *hammurabi* to create maps of Stokes parameters, but these were not directly compared to observations. Instead, for synchrotron and dust emission, they multiplied an observed total intensity template by the simulated polarization fraction in order to simulate the polarization data. This means that the assumed particle distributions did not have to be very accurate, and yet the resulting simulation of polarization could be made to match well. In order to unambiguously constrain the large-scale properties of the field, however, we prefer to directly compare the morphologies of models and data.



(a) LFI 30 GHz  $P$



(b) Jansson12b 30 GHz  $P$



(c) Jaffe13b 30 GHz  $P$

**Fig. 10.** Zooms centred on the inner Galactic region (in a Gnomonic projection with a  $10^\circ$  grid) for the  $P$  of the data (top) and two of the models (one realization of each). The dashed lines are the spurs and loops as in Fig. 9. (Recall that in the profile plots, the region where  $|l| < 10^\circ$  and  $|b| < 10^\circ$  is masked.)

##### 4.1. Dust distribution and polarization properties

For the computation of the thermal dust emission, we require a model for the spatial distribution of the dust. We start from the dust distribution model of Jaffe13, which is similar to that of [Drimmel & Spergel \(2001\)](#) in its parametrization. The parameters required updating, particularly the scale heights, which had not been constrained in Jaffe13, since that analysis was confined to the plane.

We find that using that parametrization with two scale heights, one for a thicker axisymmetric component and one for a narrower spiral arm component, fits the low-latitude emission but overpredicts the emission for  $|b| \gtrsim 30^\circ$ . This is likely due to the absence of dust emission in the Solar neighbourhood studied by, e.g., [Lallement et al. \(2014\)](#) and references therein. We therefore add a feature to our dust distribution: a cylinder centred on the Sun's position with a configurable radius, height, and dust density damping fac-

tor. We set the dust density to zero within a region of 150 pc in radius and 200 pc in height. This cylinder is a crude approximation to the “local bubble”, a tilted low-density region studied in [Lallement et al. \(2014\)](#). The amount of dust left in this region relative to the large-scale model is largely degenerate with its extent, and we do not attempt a detailed modelling here. This is the only such small-scale structure in the model, but it is apparently necessary because of the large effect such a local structure can have on the high-latitude sky. Elsewhere, the model is effectively an average over a Galaxy full of such small-scale structures that the analysis is not sensitive to.

We also adjust several parameters to fit the longitude profile of the dust intensity along the plane because the morphology is not quite the same at 353 GHz (used here) as at 94 GHz (used in [Jaffe13](#)). In particular, we damp the two outer arms relative to the two inner arms, and we reduce the scale radii for both the smooth and spiral arm components.

This leads to the model that approximately matches the data, as shown in [Figs. 11 through 13](#). As with the magnetic field models, a complete exploration of the parameter space is not performed here. This would, for example, improve the locations and amplitudes of the shoulder-features in the longitude profiles seen in [Fig. 12](#). This distribution would be interesting to compare to the original [Drimmel & Spergel \(2001\)](#) model, since the older model was based on IRAS data at higher frequencies, and as we see in [M31 \(Planck Collaboration Int. XXV 2015\)](#), the apparent profile of the dust emission depends on frequency. The analysis here, however, is not sensitive to the details of this distribution, since the uncertainties in the magnetic field modelling are larger than the uncertainties in the dust distribution. This approximate model is sufficient to study the degree of polarization and the implications for the magnetic fields towards the inner Galaxy. The outer Galaxy latitude profiles show that the model is too narrow, but we focus on the inner Galaxy, where we are looking through most of the disc.

We give an updated table of our dust model parameters in [Table C.2](#).

The polarization is modelled as described by [Fauvet12](#), where the degree of polarization drops with the angle to the LOS,  $\alpha$ , as  $\sin^2 \alpha$ . In this case, we omit the additional factor of  $\sin \alpha$  that was used there as an approximation for grain misalignment, but it does not make a significant difference to the results. The intrinsic (i.e., sub-grid) polarization fraction is set to 20% following the results of [Planck Collaboration Int. XIX \(2015\)](#). This is the lower limit for the *maximum* polarization fraction observed in the diffuse emission by *Planck*. In our modelling, this parameter folds in all sub-grid effects, i.e., any variations in the polarization properties on small scales and any correlations between the polarization properties and the dust density or emissivity. This parameter is a large systematic uncertainty in the analysis and can effectively scale the polarization independently of all other parameters.

#### 4.2. Dust predictions from synchrotron-based models

[Figures 11 and 12](#) show latitude and longitude profiles, while [Fig. 13](#) compares the maps.

#### 4.2.1. Profiles and large-scale features

The latitude profiles in the inner Galaxy shown in [Fig. 11](#) (top) show that the predicted total intensity (left) has approximately the right thin-disc thickness in the inner Galaxy for  $|b| \lesssim 10^\circ$ , but the polarized intensity (right) is too narrow. The synchrotron profiles in [Fig. 4](#) show no such disparity, so this mismatch in the dust polarization must then be due to a change in the magnetic fields in the narrow disc where the dust is found but where the synchrotron is less sensitive.

The dust intensity in the outer Galaxy ([Fig. 11](#) bottom) is also mis-matched in polarization at low latitudes, but because it is less well matched in total intensity and in synchrotron emission in this region, we cannot draw any conclusions there.

If this difference is significant (which depends on the expected GV, a function of the field ordering, in turn a function of the component separation, etc.) then it points to a problem in the degree of field ordering in the model as a function of height in the thin disc. The model may be correct on the larger scales probed by the thick synchrotron disc and yet have too thinly distributed an ordered field component in the disc as traced by the dust.

At intermediate to high latitudes ( $|b| \gtrsim 10^\circ$ ), all models underpredict significantly the polarized intensity of dust.

As in [Jaffe13](#), the longitude profiles along the Galactic plane show that the inner regions of the Galaxy ( $-30^\circ \lesssim l \lesssim 30^\circ$ ) are overpredicted in polarization for some of the models. Unlike in that work, however, some updated models can be made to reproduce roughly the right level of polarization emission in parts of the outer Galaxy. (The [Jansson12](#) model shows the most extreme case where the fields are completely ordered in much of the dust-emitting regions, and this then overpredicts the polarization toward the anti-centre.) Again, this is due to the changes in the degree of field ordering that are necessary to fit to the [Commander](#) synchrotron solution discussed above. Since it is not clear that this change is physically realistic, it is possible that the fields are more disordered than in our current models tailored to this synchrotron estimate. It is therefore not clear that the mismatch discussed by [Jaffe13](#) between the degree of polarization in the dust and synchrotron emission in the plane has been resolved.

These issues will be discussed further in [Sect. 4.4](#).

#### 4.2.2. Maps and local residuals

The left column and fifth row of [Fig. 13](#) shows the residuals for the model dust prediction compared to the 353 GHz data in total intensity. Since dust total  $I$  is not a function of the magnetic field, what is seen is only the distribution of the dust emissivity model as described in [Sect. 4.1](#). For the significance of the residuals, we divide by the sky rms estimate of the galactic variance (see [Sect. 3.4.1](#)) computed on the dust total intensity map.

The residual map in total intensity highlights several known nearby regions by removing the background Galactic disc. For example, above the Galactic centre is a strong arc of emission from the Aquila Rift up through the Ophiuchus region. Since the dust is in the thin disc, the emission at  $|b| > 10^\circ$  is very close and included in the Gould Belt system as determined using HI velocities and mapped by [Lallement et al. \(2014\)](#). The Aquila Rift, for instance, is



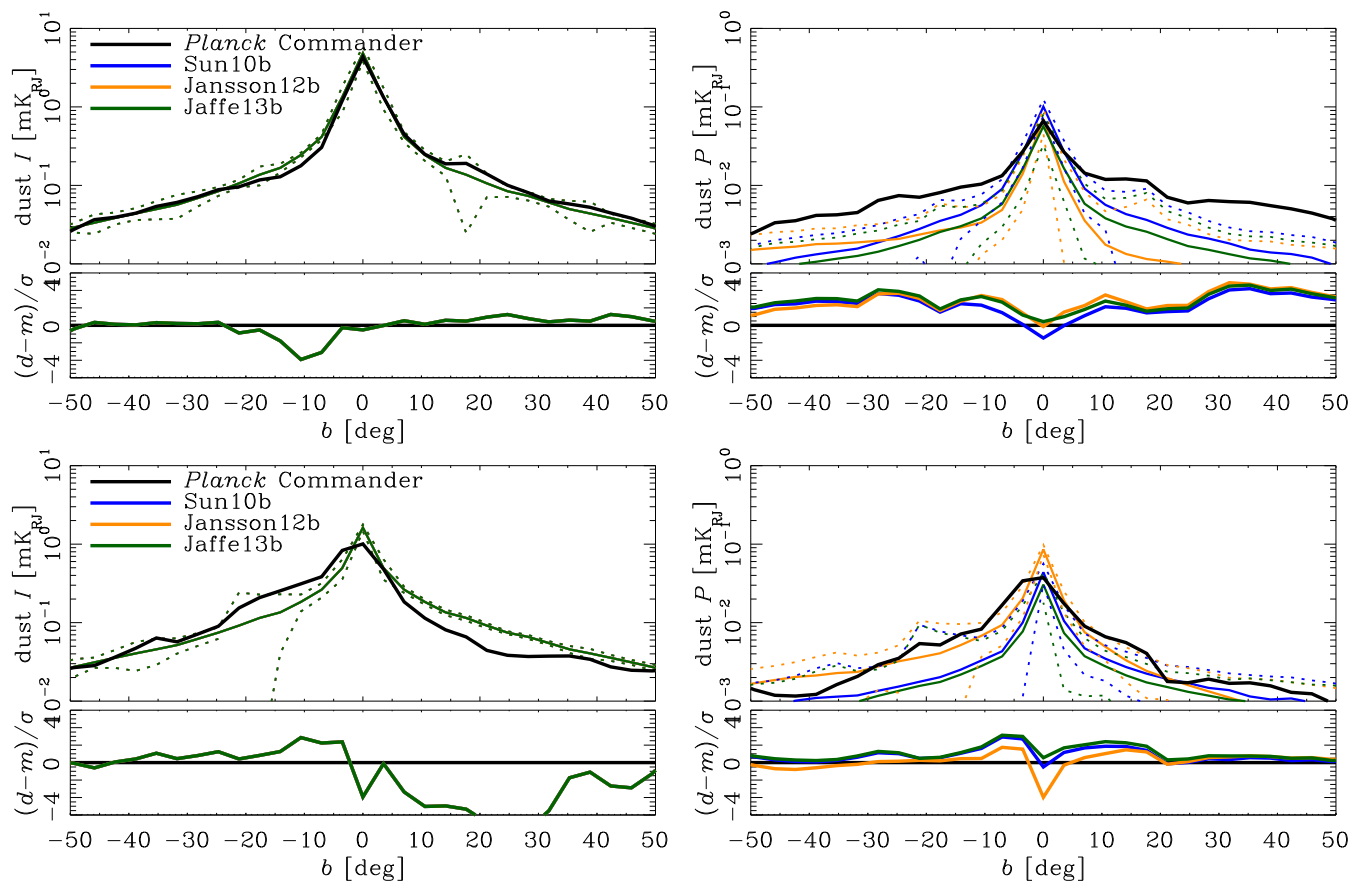


**Fig. 11.** Dust profiles in latitude for the models as in Fig. 4. The top shows the inner Galaxy (i.e.,  $-90^\circ < l < 90^\circ$ ), while the bottom shows the third quadrant ( $180^\circ < l < 270^\circ$ , i.e., the outer Galaxy excluding the Fan region). For total intensity on the left, the **Commander** dust solution in solid black is compared to the *Planck* 2013 dust model of [Planck Collaboration XI \(2014\)](#) (black dashed), but the difference is not generally visible. (Since the models shown in colour differ only in the magnetic field, which has no impact on the dust total intensity, these curves are not distinguishable.)

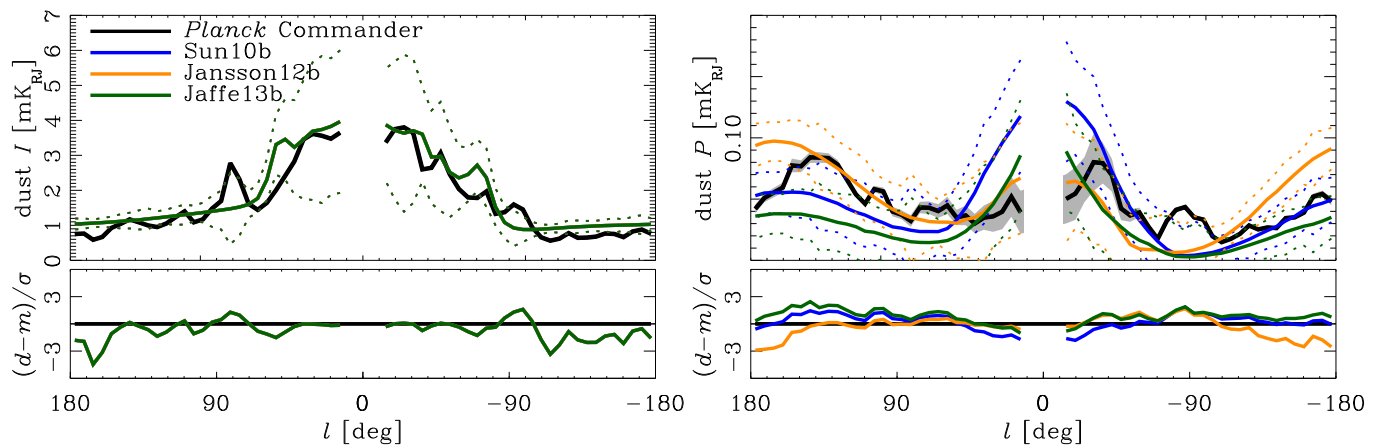


**Fig. 12.** Dust profiles in longitude for the updated models in Fig. 11. The grey band shows the uncertainty in the data due to the bandpass leakage discussed in Sect. A.2.

known to be about 80 to 100 pc away (see, e.g., the starlight polarimetry of [Santos et al. 2011](#)). This is clearly on the “wall” of the local cavity, possibly also on the swept-up shell of Loop I (even if its centre is at the larger distance as per [Planck Collaboration Int. XXV 2015](#)). We also see that the intensity minima are not at the Galactic poles but tilted, which is consistent with the tilted local “chimney” from [Lallement et al. \(2014\)](#).

The Fan region is also quite distinctly visible near the plane in the second quadrant. The model for the dust distribution includes spiral arm components, so this map shows how the Fan region is bright in dust emission even on top of the prediction from the Perseus arm ridge.

In polarization, these residuals pick out strongly some of the features visible in [Planck Collaboration Int. XIX \(2015\)](#) such as the strong diagonal stretch of Stokes  $U$ , im-

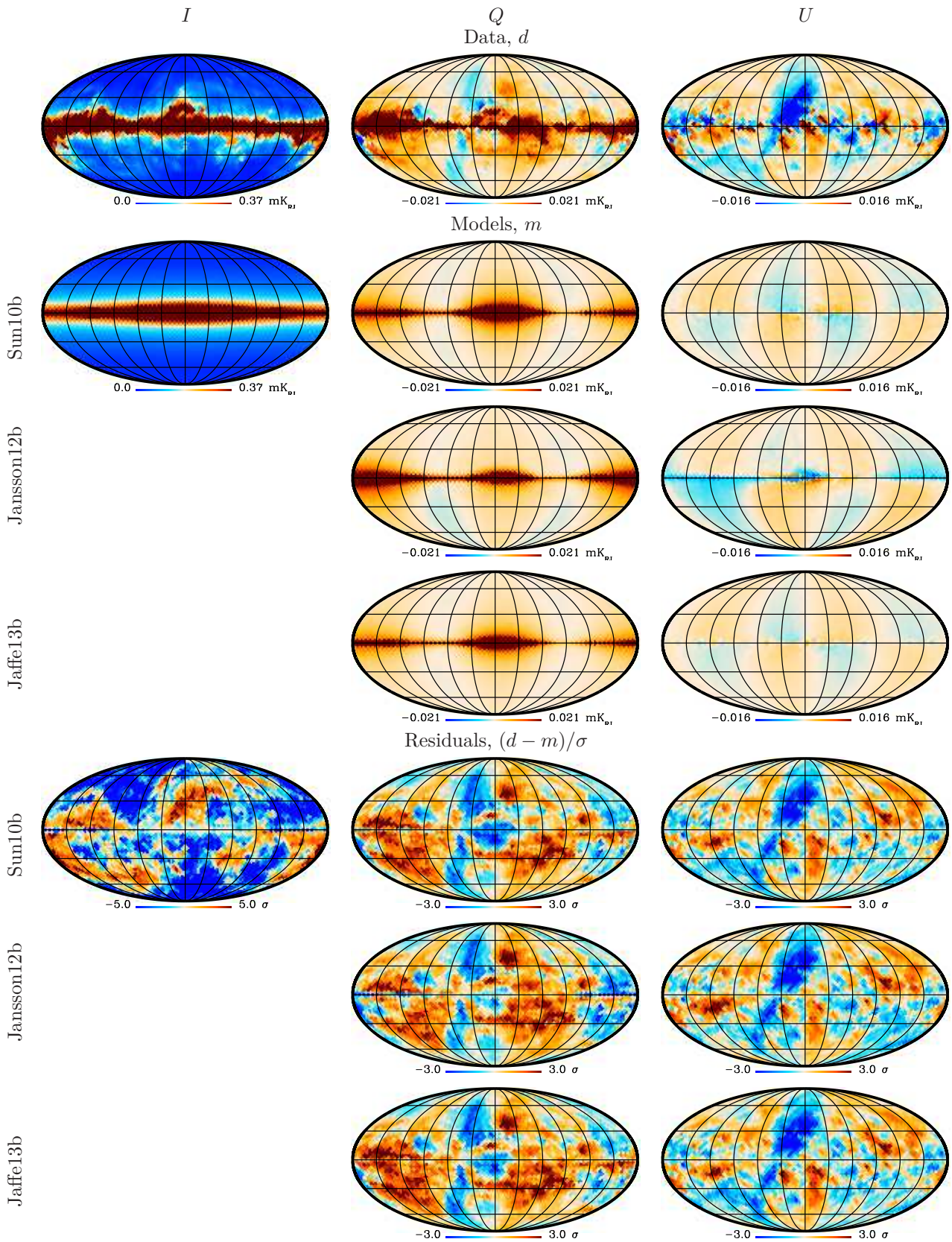


**Fig. 13.** Comparison of the model predictions for dust and the *Planck* data. The columns from left to right are for Stokes  $I$ ,  $Q$ , and  $U$ , while the rows are the data followed by the prediction for each model, and lastly the difference between model and data divided by the uncertainty. As for synchrotron emission, the polarization uncertainty is computed as the ensemble variance predicted by the models. Since dust total intensity is not a function of the magnetic field, its uncertainties are computed from the sky rms of the dust map.

plying that the magnetic field is somewhat aligned along this feature. This structure is not only associated with the arc above the Galactic centre but also appears to continue eastwards below the plane. The Fan region is also quite bright and not accounted for by the spiral arm model of the dust distribution or the magnetic fields.

These structures are well inside the outer scale of the magnetic field turbulence and cannot be modelled by the methods we use here.

#### 4.3. Jansson12c: a dust-based magnetic field model

All models optimized for synchrotron underpredict dust polarization for  $|b| \gtrsim 5^\circ$ . This is despite the fact that the latitude profile of the dust total intensity matches observations, and the synchrotron latitude profiles match in both total and polarized intensities. As discussed by Jaffe13, one degeneracy in the synchrotron modelling is the precise relative distributions of the coherent and random fields. The CRL distribution is thought to be fairly smooth, while the dust is thought to be concentrated in a thin disc with annular and spiral arm modulations. (This has been modelled in the Milky Way by Drimmel & Spergel 2001 and can be seen directly in *Planck* observations of M31 in Planck Collaboration Int. XXV 2015.) Therefore, the dust polarization can be used to study precisely where the magnetic fields are more or less ordered relative to these arms and relative to the mid-plane of the Galaxy.

We choose to use the Jansson12 model because it has an easy parametrization for distinct morphological components of the coherent and random fields, particularly the disc, halo, and x-shaped components and the spiral segments. The high-latitude dust polarization is a function of what is going on in both the local arm segment (we are situated near the inner side of segment five) and the next segment inward (number four, which dominates the high-latitude sky looking towards the inner Galaxy). One peculiarity of this model is the presence of jumps between different spiral segments in the narrow disc and between the narrow disc and the thick-disc toroidal component. The dust latitude profiles towards the inner and outer Galaxy are each very sensitive to the details of these transitions because the dust is so narrowly distributed and therefore all emission above  $10^\circ$  is very local. (This is not the case for synchrotron, which is not as sensitive to these properties.) In order to simplify the adjustments needed to match the data, we shift the arm pattern slightly so that the region around the observer is located fully within segment five and segment four does not impact the high-latitude emission.

As shown in Fig. 11, the Jansson12b model developed to match synchrotron underpredicts the polarization at high latitudes, as do all the models. We therefore decrease the random component in the local arm segment (number five) and increase its coherent field amplitude in order to increase the intermediate-latitude polarized intensity. The synchrotron comes from a much thicker region, so it is more dependent on the toroidal thick-disc component and does not change significantly with this adjustment.

We refer to these further adjustments as “Jansson12c” in Fig. 14. It is clear that a thorough exploration of the parameter space would find a better model to fit all of the available data, but the point of our Jansson12c model is not to present the definitive solution to the problem; it is to show how the dust and synchrotron can be used together to

reduce, though not eliminate, degeneracies in the parameter space.

#### 4.4. Outstanding issues

Since neither the Jansson12b model adjusted to match synchrotron nor the Jansson12c model adjusted to match the dust is a best-fit model, their utility is primarily as examples of how synchrotron and dust can be used to probe the fields in the thin and thick discs traced by the two components with very different scale heights. These methods, however, are only as reliable as the observations on which they are based, and they are of course affected by local structures that the models cannot take into account. The differences between the two models are motivated by the fact that the synchrotron predictions of the first model match the data profiles as a function of latitude, but the dust profiles do not. It is not clear, however, how certain this mismatch is and therefore whether either this scenario or the “fix” in Jansson12c is realistic.

The main limitation of this analysis, as discussed above, is the uncertainty in the synchrotron spectrum, which is thought to harden in the Galactic plane in a way not accounted for here. If the component-separation procedure included such a spectral hardening near the plane (e.g., based on additional information from additional surveys at GHz frequencies), then this would increase the predicted synchrotron total intensity in the plane. (There would then be a corresponding decrease in the ill-constrained AME component.) This in turn would require a *decrease* in the degree of magnetic field ordering near the plane relative to high latitudes. Such a model in the plane would resemble that of Jaffe13, which assumed a similar synchrotron spectrum. That work shows that this assumption leads to an underprediction of the dust polarization in the plane.

Once the 3D magnetic field models were adjusted to match such a model of varying synchrotron spectrum, the latitude profile of dust polarization would be less peaked. The model would underpredict for all latitudes, though the precise shape of the profile would depend on that of the varying synchrotron spectrum. The entire curve could be shifted up to match the data by increasing the sub-grid dust polarization fraction. That parameter is currently set at 20% but is highly uncertain and, as mentioned above, is a lower limit on the maximum.

This line of reasoning suggests two things. Firstly, the polarized dust emission that is very peaked near the plane may be an artefact of the uncertain component separation and synchrotron spectral index. In other words, it may not be real. Secondly, the high degree of dust polarization predicted by the models in the Galactic plane may also not be real. It is therefore not clear whether the problem described by Jaffe13 (the difficulty reproducing the high level of dust polarization in the plane) remains or whether the Jansson12c model is roughly correct. As discussed in Sect. 3.4.2, a variation in the synchrotron spectrum is supported by other observations of (and plausible reasons for) a hardening of the synchrotron index in the plane, but it would contribute to the problem of underpredicted dust polarization by decreasing the dust polarization in the plane unless renormalized. The increase in the intrinsic dust polarization fraction required to match the data with more disordered fields in the plane would be quite large, at least a factor of two, which is unlikely given that even relatively



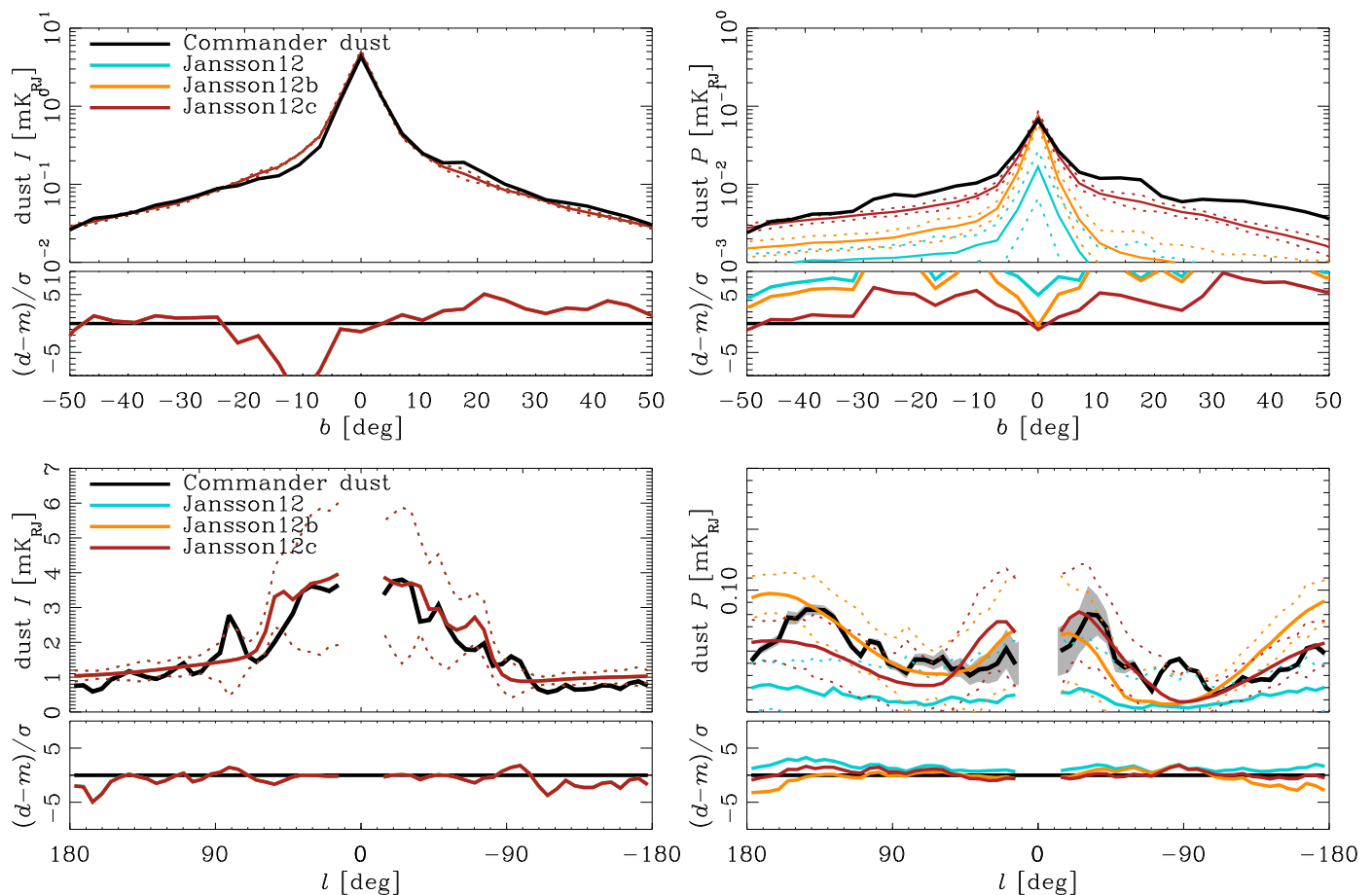


**Fig. 14.** Dust latitude profiles for the three Jansson12 models. The top shows the inner Galaxy (i.e.,  $-90^\circ < l < 90^\circ$ ), while the bottom shows the longitude profile along the Galactic plane.

nearby isolated clouds do not approach such values; see, e.g., [Planck Collaboration Int. XIX \(2015\)](#). In short, these problems remain unresolved, and the discrepancy between the synchrotron and dust polarization degrees is likely to require a more sophisticated model for the ordering of the magnetic fields in the thin and thick discs.

Recall also that in order to fit the latitude profile of the dust total intensity, we implemented a model for the local bubble as a cavity of radius 150 pc and height 200 pc with no dust inside. Since the dust is confined to a very narrow disc, this removes most of the dust in the Solar neighbourhood, but there remains high-latitude dust clearly visible in the logarithmic latitude profile in total intensity, and yet this emission is not strongly polarized in the models. Those models do not include any effect on polarization of such a bubble. One could imagine a scenario wherein the process that created the local bubble and evacuated much of the dust from the solar neighbourhood also left a shell of ordered magnetic fields that might retain enough dust to explain this mismatch. Such a local phenomenon would not be reflected in the synchrotron emission that traces a much thicker disc. To resolve this will require further observations that constrain the dust and field distributions in the solar neighbourhood, such as using the velocity information from HI observations, in addition to more local starlight polarization measurements.

Lastly, we see that the inner plane is not well fitted in either synchrotron or dust emission. For  $10^\circ \lesssim |l| \lesssim 20^\circ$ , the models have a roughly similar synchrotron amplitude on average, but it is apparent that the polarized synchrotron emission here is climbing rapidly in a way that the models do not reflect. By contrast, the dust polarization is overestimated by most models in this region. We do not attempt to model the innermost Galaxy, but clearly the modelling of the region within the molecular ring is incorrect. This is a complicated region likely affected by the Galactic bar, changes in the star formation, etc. A study focused on this region comparing synchrotron and dust would be extremely interesting for future work.

## 5. Conclusions

We have updated three models for the Galactic magnetic fields in the literature (Sun10, Jansson12, and Jaffe13) in order to match the *Planck* Commander synchrotron maps. We use a common CRL model from Orlando13, which has different spatial and spectral behaviour than the CRL models used in the original development of each of the magnetic field models. Different CRL models result in changes to both the morphology of the predicted synchrotron emission and the inferred degree of field ordering. The reference synchrotron data also have a different morphology from, e.g., the WMAP component-separation products used in

developing the Jansson12 model. For these reasons, all of the field models required adjustments to their parameters in order to match. Our updates are neither best-fit models nor unique solutions in a degenerate parameter space, but a full exploration of these parameters is beyond the scope of this work. Nevertheless, the updated models roughly reproduce the basic large-scale morphology of the synchrotron emission in total and polarized intensity as measured by *Planck*.

One of the results of this paper is to demonstrate explicitly how the choice of CRL model (particularly the spectrum) and the component separation in the microwave bands (which is related) affect the results. Such issues are also discussed in [Planck Collaboration XXV \(2016\)](#), and here we show how they affect in particular the estimates for the degree of polarization in the synchrotron emission and therefore the degree of ordering in the magnetic fields. We use the *Planck* component separation results, but these are subject to uncertainties and are unlikely to be reliable estimates in the Galactic plane, where we are attempting to probe the magnetic fields through the full Galactic disc. The resulting models, like all of the models in the literature, are therefore still subject to significant uncertainties because of these issues, as will be the case for any such analysis using the *Planck* synchrotron estimate.

With the updated magnetic field models, we turn to the predictions for polarized dust emission and compare them with the *Planck* data at 353 GHz. We find that the predictions do not match the dust emission well, whether using the original magnetic field models from the literature or our updated models. In particular, all of the models predict a narrower distribution of polarized dust emission in the plane than is observed by *Planck* and underpredict the polarized emission away from the plane. Because the synchrotron component separation is uncertain, as are the synchrotron spectral index and its latitude variation, the vertical variation in the magnetic field ordering is also uncertain. That uncertainty also affects the latitude variation of the dust polarization, so this issue is far from understood.

We then further adjust the Jansson12 model parameters in a way that remains consistent with the synchrotron emission but is also a closer match to the dust polarization. This is meant as a proof of concept, rather than as a physically well-motivated model, and illustrates how we can, in principle, probe the different fields traced by these two components. Though this model remains subject to the uncertainties discussed extensively in this work, the update nevertheless represents the most comprehensive effort to model the large-scale Galactic magnetic fields using the combination of Faraday RM data, diffuse synchrotron emission, and the new thermal dust polarization information brought by the *Planck* data.

Previous analyses have proceeded from different assumptions about component separation and/or about the synchrotron spectral index, and this has led to very different models for the large-scale fields providing adequate matches to the chosen subsets of the available data. We have compared these models with each other and updated them for a particular set of assumptions, i.e., those made in the *Planck* component separation, but we have not overcome these problems. The main result of this paper is an improved understanding of the challenges in the analysis and of the limitations of the existing models.

There are, however, several specific points that we have established:

- The original Jansson12 model clearly has too large a random component, likely due to the WMAP MCMC solution being contaminated by AME. This is indicated by the total amount of synchrotron emission and by the significantly overpredicted galactic variance for synchrotron polarization.
- Our updated models may, in contrast, underestimate this random component. This is implied by the observed versus modelled variations and may be explained by the fact that the *Planck Commander* analysis assumes a very steep synchrotron spectrum. This question remains unanswered, and the original Jansson12 model and our updates likely represent the extremes that bracket reality.
- When using the field models adjusted to match the *Commander* synchrotron solution, i.e., with the assumed steep synchrotron spectrum and the correspondingly strongly ordered magnetic field model, the predicted dust polarization matches roughly the level of polarization in the outer regions of the Galactic plane, or can even be made to overpredict it. This is in contrast to the results of Jaffe13 but is clearly dependent on the outstanding component separation question.
- We can adjust the Jansson12 model to roughly match both synchrotron and dust emission. This model depends strongly on choices made in the component-separation process but demonstrates how the addition of polarized dust emission can improve the detailed modelling in the thin Galactic disc.

The prospects for large-scale magnetic field modelling are quite promising. Firstly, ongoing ground-based radio surveys (see Appendix B) will soon map the sky at several crucial intermediate frequencies and provide leverage for component-separation algorithms such as *Commander* via the additional information about the synchrotron spectrum at low frequencies. In the longer term, the Square Kilometre Array (SKA<sup>18</sup>) will increase the sampling of Galactic pulsars by several orders of magnitude, which will improve our understanding of both the thermal electron distribution and the magnetic fields in the narrow disc component. The Gaia mission<sup>19</sup> will provide millions of extinction measurements in the local quadrant of the Galaxy that will allow more precise mapping of the dust distribution. The combination of SKA and Gaia will therefore greatly advance our ability to study the fields in the thin disc. SKA will also improve the sampling of the extragalactic sources that trace the fields throughout the Galaxy, including the halo. The combination of all of these data will help to study precisely this question of how the RM data, synchrotron emission, and dust emission reveal the different regions of the magnetized ISM.

*Acknowledgements.* The Planck Collaboration acknowledges the support of: ESA; CNES, and CNRS/INSU-IN2P3-INP (France); ASI, CNR, and INAF (Italy); NASA and DoE (USA); STFC and UKSA (UK); CSIC, MINECO, JA and RES (Spain); Tekes, Aof, and CSC (Finland); DLR and MPG (Germany); CSA (Canada); DTU Space (Denmark); SER/SSO (Switzerland); RCN (Norway); SFI (Ireland); FCT/MCTES (Portugal); ERC and PRACE (EU). A description of the Planck Collaboration

<sup>18</sup> <https://www.skatelescope.org/>

<sup>19</sup> <http://sci.esa.int/gaia/>

and a list of its members, indicating which technical or scientific activities they have been involved in, can be found at <http://www.cosmos.esa.int/web/planck/planck-collaboration>. Some of the results in this paper have been derived using the HEALPix package. We acknowledge the use of the Legacy Archive for Microwave Background Data Analysis (LAMBDA), part of the High Energy Astrophysics Science Archive Center (HEASARC). HEASARC/LAMBDA is a service of the Astrophysics Science Division at the NASA Goddard Space Flight Center.

## References

- Abdo, A. A., Ackermann, M., Ajello, M., et al., Fermi Observations of Cassiopeia and Cepheus: Diffuse Gamma-ray Emission in the Outer Galaxy. 2010, *ApJ*, 710, 133
- Ackermann, M., Ajello, M., Atwood, W. B., et al., Fermi LAT observations of cosmic-ray electrons from 7 GeV to 1 TeV. 2010, *Phys. Rev. D*, 82, 092004
- Beck, R., Magnetic Fields in Spiral Galaxies. 2015, [arXiv:1509.04522](https://arxiv.org/abs/1509.04522)
- Boudaud, M., Aupetit, S., Caroff, S., et al., A new look at the cosmic ray positron fraction. 2015, *A&A*, 575, A67
- Brown, J. C. & Taylor, A. R., The Structure of the Magnetic Field in the Outer Galaxy from Rotation Measure Observations through the Disk. 2001, *ApJ*, 563, L31
- Carretti, E., Crocker, R. M., Staveley-Smith, L., et al., Giant magnetized outflows from the centre of the Milky Way. 2013, *Nature*, 493, 66
- Cordes, J. M. & Lazio, T. J. W., NE2001.I. A New Model for the Galactic Distribution of Free Electrons and its Fluctuations. 2002, preprint (astro-ph/0207156)
- Drimmel, R. & Spergel, D. N., Three-dimensional Structure of the Milky Way Disk: The Distribution of Stars and Dust beyond 0.35  $R_{M\odot}$ . 2001, *ApJ*, 556, 181
- Fauvet, L., Macias-Pérez, J. F., Aumont, J., et al., Joint 3D modelling of the polarized Galactic synchrotron and thermal dust foreground diffuse emission. 2011, *A&A*, 526, 145
- Fauvet, L., Macias-Perez, J. F., Jaffe, T. R., et al., Expected constraints on the Galactic magnetic field using Planck data. 2012, *A&A*, 540, A122
- Fuskeland, U., Wehus, I. K., Eriksen, H. K., & Næss, S. K., Spatial Variations in the Spectral Index of Polarized Synchrotron Emission in the 9 yr WMAP sky Maps. 2014, *ApJ*, 790, 104
- Gaggero, D., Maccione, L., Grasso, D., Di Bernardo, G., & Evoli, C., PAMELA and AMS-02  $e^+$  and  $e^-$  spectra are reproduced by three-dimensional cosmic-ray modeling. 2014, *Phys. Rev. D*, 89, 083007
- Génova-Santos, R., Martín, J. A. R., Rebolo, R., et al., QUIJOTE scientific results - I. Measurements of the intensity and polarisation of the anomalous microwave emission in the Perseus molecular complex. 2015, *MNRAS*, 452, 4169
- Gold, B., Odegard, N., Weiland, J. L., et al., Seven-year Wilkinson Microwave Anisotropy Probe (WMAP) Observations: Galactic Foreground Emission. 2011, *ApJS*, 192, 15
- Górski, K. M., Hivon, E., Banday, A. J., et al., HEALPix: A Framework for High-Resolution Discretization and Fast Analysis of Data Distributed on the Sphere. 2005, *ApJS*, 622, 759
- Grenier, I. A., Black, J. H., & Strong, A. W., The Nine Lives of Cosmic Rays in Galaxies. 2015, *ARA&A*, 53, 199
- Han, J. L., Manchester, R. N., Lyne, A. G., Qiao, G. J., & van Straten, W., Pulsar Rotation Measures and the Large-Scale Structure of the Galactic Magnetic Field. 2006, *ApJ*, 642, 868
- Haslam, C. G. T., Salter, C. J., Stoffel, H., & Wilson, W. E., A 408 MHz all-sky continuum survey. II - The atlas of contour maps. 1982, *A&AS*, 47, 1
- Haverkorn, M. 2014, in *Magnetic Fields in Diffuse Media*, ed. E. M. de Gouveia Dal Pino & A. Lazarian (Berlin, Heidelberg: Springer Berlin Heidelberg), 483–506
- Haverkorn, M. & Spangler, S. R., Plasma Diagnostics of the Interstellar Medium with Radio Astronomy. 2013, *Space Sci Rev*, 178, 483
- Jaffe, T. R., Banday, A. J., Leahy, J. P., Leach, S., & Strong, A. W., Connecting synchrotron, cosmic rays and magnetic fields in the plane of the Galaxy. 2011, *MNRAS*, 416, 1152
- Jaffe, T. R., Ferrière, K. M., Banday, A. J., et al., Comparing polarized synchrotron and thermal dust emission in the Galactic plane. 2013, *MNRAS*, 431, 683
- Jaffe, T. R., Leahy, J. P., Banday, A. J., et al., Modelling the Galactic magnetic field on the plane in two dimensions. 2010, *MNRAS*, 401, 1013
- Jansson, R. & Farrar, G. R., A New Model of the Galactic Magnetic Field. 2012a, *ApJ*, 757, 14
- Jansson, R. & Farrar, G. R., The Galactic Magnetic Field. 2012b, *ApJL*, 761, L11
- King, O. G., Jones, M. E., Blackhurst, E. J., et al., The C-Band All-Sky Survey (C-BASS): design and implementation of the northern receiver. 2014, *MNRAS*, 438, 2426
- Lallement, R., Vergely, J. L., Valette, B., et al., 3D maps of the local ISM from inversion of individual color excess measurements. 2014, *A&A*, 561, A91
- Lawson, K. D., Mayer, C. J., Osborne, J. L., & Parkinson, M. L., Variations in the Spectral Index of the Galactic Radio Continuum Emission in the Northern Hemisphere. 1987, *MNRAS*, 225, 307
- Orlando, E. & Strong, A., Galactic synchrotron emission with cosmic ray propagation models. 2013, *MNRAS*, 436, 2127
- Page, L., Hinshaw, G., Komatsu, E., et al., Three-Year Wilkinson Microwave Anisotropy Probe (WMAP) Observations: Polarization Analysis. 2007, *ApJS*, 170, 335
- Planck Collaboration XI, *Planck* 2013 results. XI. All-sky model of thermal dust emission. 2014, *A&A*, 571, A11, [arXiv:1312.1300](https://arxiv.org/abs/1312.1300)
- Planck Collaboration I, *Planck* 2015 results. I. Overview of products and results. 2016, *A&A*, submitted, [arXiv:1502.01582](https://arxiv.org/abs/1502.01582)
- Planck Collaboration II, *Planck* 2015 results. II. Low Frequency Instrument data processing. 2016, *A&A*, submitted, [arXiv:1502.01583](https://arxiv.org/abs/1502.01583)
- Planck Collaboration VI, *Planck* 2015 results. VI. LFI maps. 2016, *A&A*, submitted, [arXiv:1502.01585](https://arxiv.org/abs/1502.01585)
- Planck Collaboration VII, *Planck* 2015 results. VII. High Frequency Instrument data processing: Time-ordered information and beam processing. 2016, *A&A*, in press, [arXiv:1502.01586](https://arxiv.org/abs/1502.01586)
- Planck Collaboration VIII, *Planck* 2015 results. VIII. High Frequency Instrument data processing: Calibration and maps. 2016, *A&A*, in press, [arXiv:1502.01587](https://arxiv.org/abs/1502.01587)
- Planck Collaboration X, *Planck* 2015 results. X. Diffuse component separation: Foreground maps. 2016, *A&A*, submitted, [arXiv:1502.01588](https://arxiv.org/abs/1502.01588)
- Planck Collaboration XXV, *Planck* 2015 results. XXV. Diffuse, low-frequency Galactic foregrounds. 2016, *A&A*, submitted, [arXiv:1506.06660](https://arxiv.org/abs/1506.06660)
- Planck Collaboration Int. XIX, *Planck* intermediate results. XIX. An overview of the polarized thermal emission from Galactic dust. 2015, *A&A*, 576, A104, [arXiv:1405.0871](https://arxiv.org/abs/1405.0871)
- Planck Collaboration Int. XXIII, *Planck* intermediate results. XXIII. Galactic plane emission components derived from Planck with ancillary data. 2015, *A&A*, 580, A13, [arXiv:1406.5093](https://arxiv.org/abs/1406.5093)
- Planck Collaboration Int. XXV, *Planck* intermediate results. XXV. The Andromeda Galaxy as seen by *Planck*. 2015, *A&A*, 582, A28, [arXiv:1407.5452](https://arxiv.org/abs/1407.5452)
- Prouza, M. & Šmída, R., The Galactic magnetic field and propagation of ultra-high energy cosmic rays. 2003, *A&A*, 410, 1
- QUIET Collaboration, Ruud, T. M., Fuskeland, U., et al., The Q/U Imaging Experiment: Polarization Measurements of the Galactic Plane at 43 and 95 GHz. 2015, *ApJ*, 811, 89
- Remazeilles, M., Dickinson, C., Banday, A. J., Bigot-Sazy, M. A., & Ghosh, T., An improved source-subtracted and destriped 408 MHz all-sky map. 2014, *arXiv*, [arXiv:1411.3628v1](https://arxiv.org/abs/1411.3628v1)
- Ruiz-Granados, B., Rubino-Martin, J. A., & Battaner, E., Constraining the regular Galactic magnetic field with the 5-year WMAP polarization measurements at 22 GHz. 2010, *A&A*, 522, A73
- Santos, F. P., Corradi, W., & Reis, W., Optical Polarization Mapping Toward the Interface Between the Local Cavity and Loop I. 2011, *ApJ*, 728, 104
- Stanev, T., Ultra-high-energy Cosmic Rays and the Large-scale Structure of the Galactic Magnetic Field. 1997, *ApJ*, 479, 290
- Strong, A., Porter, T., Digel, S., et al., Global Cosmic-ray-related Luminosity and Energy Budget of the Milky Way. 2010, *ApJ*, 722, L58
- Strong, A. W., Moskalenko, I. V., & Ptuskin, V. S., Cosmic-Ray Propagation and Interactions in the Galaxy. 2007, *Annual Review of Nuclear and Particle Science*, 57, 285
- Strong, A. W., Orlando, E., & Jaffe, T. R., The interstellar cosmic-ray electron spectrum from synchrotron radiation and direct measurements. 2011, *A&A*, 534, 54
- Sun, X.-H. & Reich, W., The Galactic halo magnetic field revisited. 2010, *Res. Astron. Astrophys.*, 10, 1287



- Sun, X. H., Reich, W., Waelkens, A., & Enßlin, T. A., Radio observational constraints on Galactic 3D-emission models. 2008, *A&A*, 477, 573
- Uyaniker, B., Landecker, T. L., Gray, A. D., & Kothes, R., Radio Polarization from the Galactic Plane in Cygnus. 2003, *ApJ*, 585, 785
- Vidal, M., Dickinson, C., Davies, R. D., & Leahy, J. P., Polarized radio filaments outside the Galactic plane. 2015, *MNRAS*, 452, 656
- Waelkens, A., Jaffe, T., Reinecke, M., Kitaura, F. S., & Enßlin, T. A., Simulating polarized Galactic synchrotron emission at all frequencies. The Hammurabi code. 2009, *A&A*, 495, 697
- Wehus, I. K., Fuskeland, U., Eriksen, H. K., et al., Monopole and dipole estimation for multi-frequency sky maps by linear regression. 2014, eprint arXiv, 7616, [arXiv:1411.7616](https://arxiv.org/abs/1411.7616)
- West, J. L., Safi-Harb, S., Jaffe, T., et al., The connection between supernova remnants and the Galactic magnetic field: A global radio study of the axisymmetric sample. 2016, *A&A*, 587, A148
- Wolleben, M., Landecker, T. L., Reich, W., & Wielebinski, R., An absolutely calibrated survey of polarized emission from the northern sky at 1.4 GHz. Observations and data reduction. 2006, *A&A*, 448, 411
- 
- <sup>1</sup> APC, AstroParticule et Cosmologie, Université Paris Diderot, CNRS/IN2P3, CEA/Irfu, Observatoire de Paris, Sorbonne Paris Cité, 10, rue Alice Domon et Léonie Duquet, 75205 Paris Cedex 13, France
- <sup>2</sup> African Institute for Mathematical Sciences, 6-8 Melrose Road, Muizenberg, Cape Town, South Africa
- <sup>3</sup> Agenzia Spaziale Italiana Science Data Center, Via del Politecnico snc, 00133, Roma, Italy
- <sup>4</sup> Astrophysics Group, Cavendish Laboratory, University of Cambridge, J J Thomson Avenue, Cambridge CB3 0HE, U.K.
- <sup>5</sup> Astrophysics & Cosmology Research Unit, School of Mathematics, Statistics & Computer Science, University of KwaZulu-Natal, Westville Campus, Private Bag X54001, Durban 4000, South Africa
- <sup>6</sup> CGEE, SCS Qd 9, Lote C, Torre C, 4° andar, Ed. Parque Cidade Corporate, CEP 70308-200, Brasília, DF, Brazil
- <sup>7</sup> CITA, University of Toronto, 60 St. George St., Toronto, ON M5S 3H8, Canada
- <sup>8</sup> CNRS, IRAP, 9 Av. colonel Roche, BP 44346, F-31028 Toulouse cedex 4, France
- <sup>9</sup> California Institute of Technology, Pasadena, California, U.S.A.
- <sup>10</sup> Centro de Estudios de Física del Cosmos de Aragón (CEFCFA), Plaza San Juan, 1, planta 2, E-44001, Teruel, Spain
- <sup>11</sup> Computational Cosmology Center, Lawrence Berkeley National Laboratory, Berkeley, California, U.S.A.
- <sup>12</sup> DSM/Irfu/SPP, CEA-Saclay, F-91191 Gif-sur-Yvette Cedex, France
- <sup>13</sup> DTU Space, National Space Institute, Technical University of Denmark, Elektrovej 327, DK-2800 Kgs. Lyngby, Denmark
- <sup>14</sup> Département de Physique Théorique, Université de Genève, 24, Quai E. Ansermet, 1211 Genève 4, Switzerland
- <sup>15</sup> Departamento de Astrofísica, Universidad de La Laguna (ULL), E-38206 La Laguna, Tenerife, Spain
- <sup>16</sup> Departamento de Física, Universidad de Oviedo, Avda. Calvo Sotelo s/n, Oviedo, Spain
- <sup>17</sup> Department of Astrophysics/IMAPP, Radboud University Nijmegen, P.O. Box 9010, 6500 GL Nijmegen, The Netherlands
- <sup>18</sup> Department of Physics & Astronomy, University of British Columbia, 6224 Agricultural Road, Vancouver, British Columbia, Canada
- <sup>19</sup> Department of Physics and Astronomy, Dana and David Dornsife College of Letter, Arts and Sciences, University of Southern California, Los Angeles, CA 90089, U.S.A.
- <sup>20</sup> Department of Physics and Astronomy, University College London, London WC1E 6BT, U.K.
- <sup>21</sup> Department of Physics, Gustaf Hällströmin katu 2a, University of Helsinki, Helsinki, Finland
- <sup>22</sup> Department of Physics, Princeton University, Princeton, New Jersey, U.S.A.
- <sup>23</sup> Department of Physics, University of California, Santa Barbara, California, U.S.A.
- <sup>24</sup> Department of Physics, University of Illinois at Urbana-Champaign, 1110 West Green Street, Urbana, Illinois, U.S.A.
- <sup>25</sup> Dipartimento di Fisica e Astronomia G. Galilei, Università degli Studi di Padova, via Marzolo 8, 35131 Padova, Italy
- <sup>26</sup> Dipartimento di Fisica e Scienze della Terra, Università di Ferrara, Via Saragat 1, 44122 Ferrara, Italy
- <sup>27</sup> Dipartimento di Fisica, Università La Sapienza, P. le A. Moro 2, Roma, Italy
- <sup>28</sup> Dipartimento di Fisica, Università degli Studi di Milano, Via Celoria, 16, Milano, Italy
- <sup>29</sup> Dipartimento di Fisica, Università degli Studi di Trieste, via A. Valerio 2, Trieste, Italy
- <sup>30</sup> Dipartimento di Matematica, Università di Roma Tor Vergata, Via della Ricerca Scientifica, 1, Roma, Italy
- <sup>31</sup> Discovery Center, Niels Bohr Institute, Blegdamsvej 17, Copenhagen, Denmark
- <sup>32</sup> Discovery Center, Niels Bohr Institute, Copenhagen University, Blegdamsvej 17, Copenhagen, Denmark
- <sup>33</sup> European Space Agency, ESAC, Planck Science Office, Camino bajo del Castillo, s/n, Urbanización Villafranca del Castillo, Villanueva de la Cañada, Madrid, Spain
- <sup>34</sup> European Space Agency, ESTEC, Keplerlaan 1, 2201 AZ Noordwijk, The Netherlands
- <sup>35</sup> Gran Sasso Science Institute, INFN, viale F. Crispi 7, 67100 L'Aquila, Italy
- <sup>36</sup> HGSFP and University of Heidelberg, Theoretical Physics Department, Philosophenweg 16, 69120, Heidelberg, Germany
- <sup>37</sup> Helsinki Institute of Physics, Gustaf Hällströmin katu 2, University of Helsinki, Helsinki, Finland
- <sup>38</sup> INAF - Osservatorio Astronomico di Padova, Vicolo dell'Osservatorio 5, Padova, Italy
- <sup>39</sup> INAF - Osservatorio Astronomico di Roma, via di Frascati 33, Monte Porzio Catone, Italy
- <sup>40</sup> INAF - Osservatorio Astronomico di Trieste, Via G.B. Tiepolo 11, Trieste, Italy
- <sup>41</sup> INAF/IASF Bologna, Via Gobetti 101, Bologna, Italy
- <sup>42</sup> INAF/IASF Milano, Via E. Bassini 15, Milano, Italy
- <sup>43</sup> INFN, Sezione di Bologna, viale Berti Pichat 6/2, 40127 Bologna, Italy
- <sup>44</sup> INFN, Sezione di Ferrara, Via Saragat 1, 44122 Ferrara, Italy
- <sup>45</sup> INFN, Sezione di Roma 1, Università di Roma Sapienza, Piazzale Aldo Moro 2, 00185, Roma, Italy
- <sup>46</sup> INFN, Sezione di Roma 2, Università di Roma Tor Vergata, Via della Ricerca Scientifica, 1, Roma, Italy
- <sup>47</sup> INFN/National Institute for Nuclear Physics, Via Valerio 2, I-34127 Trieste, Italy
- <sup>48</sup> IPAG: Institut de Planétologie et d'Astrophysique de Grenoble, Université Grenoble Alpes, IPAG, F-38000 Grenoble, France, CNRS, IPAG, F-38000 Grenoble, France
- <sup>49</sup> Imperial College London, Astrophysics group, Blackett Laboratory, Prince Consort Road, London, SW7 2AZ, U.K.
- <sup>50</sup> Infrared Processing and Analysis Center, California Institute of Technology, Pasadena, CA 91125, U.S.A.
- <sup>51</sup> Institut d'Astrophysique Spatiale, CNRS, Univ. Paris-Sud, Université Paris-Saclay, Bât. 121, 91405 Orsay cedex, France
- <sup>52</sup> Institut d'Astrophysique de Paris, CNRS (UMR7095), 98 bis Boulevard Arago, F-75014, Paris, France
- <sup>53</sup> Institute of Astronomy, University of Cambridge, Madingley Road, Cambridge CB3 0HA, U.K.
- <sup>54</sup> Institute of Theoretical Astrophysics, University of Oslo, Blindern, Oslo, Norway
- <sup>55</sup> Instituto de Astrofísica de Canarias, C/Vía Láctea s/n, La Laguna, Tenerife, Spain
- <sup>56</sup> Instituto de Física de Cantabria (CSIC-Universidad de Cantabria), Avda. de los Castros s/n, Santander, Spain

- <sup>57</sup> Istituto Nazionale di Fisica Nucleare, Sezione di Padova, via Marzolo 8, I-35131 Padova, Italy
- <sup>58</sup> Jet Propulsion Laboratory, California Institute of Technology, 4800 Oak Grove Drive, Pasadena, California, U.S.A.
- <sup>59</sup> Jodrell Bank Centre for Astrophysics, Alan Turing Building, School of Physics and Astronomy, The University of Manchester, Oxford Road, Manchester, M13 9PL, U.K.
- <sup>60</sup> Kavli Institute for Cosmology Cambridge, Madingley Road, Cambridge, CB3 0HA, U.K.
- <sup>61</sup> Kazan Federal University, 18 Kremlyovskaya St., Kazan, 420008, Russia
- <sup>62</sup> LAL, Université Paris-Sud, CNRS/IN2P3, Orsay, France
- <sup>63</sup> LERMA, CNRS, Observatoire de Paris, 61 Avenue de l'Observatoire, Paris, France
- <sup>64</sup> Laboratoire AIM, IRFU/Service d'Astrophysique - CEA/DSM - CNRS - Université Paris Diderot, Bât. 709, CEA-Saclay, F-91191 Gif-sur-Yvette Cedex, France
- <sup>65</sup> Laboratoire Traitement et Communication de l'Information, CNRS (UMR 5141) and Télécom ParisTech, 46 rue Barrault F-75634 Paris Cedex 13, France
- <sup>66</sup> Laboratoire de Physique Subatomique et Cosmologie, Université Grenoble-Alpes, CNRS/IN2P3, 53, rue des Martyrs, 38026 Grenoble Cedex, France
- <sup>67</sup> Laboratoire de Physique Théorique, Université Paris-Sud 11 & CNRS, Bâtiment 210, 91405 Orsay, France
- <sup>68</sup> Lawrence Berkeley National Laboratory, Berkeley, California, U.S.A.
- <sup>69</sup> Max-Planck-Institut für Astrophysik, Karl-Schwarzschild-Str. 1, 85741 Garching, Germany
- <sup>70</sup> Max-Planck-Institut für Extraterrestrische Physik, Giessenbachstraße, 85748 Garching, Germany
- <sup>71</sup> National University of Ireland, Department of Experimental Physics, Maynooth, Co. Kildare, Ireland
- <sup>72</sup> Nicolaus Copernicus Astronomical Center, Bartycka 18, 00-716 Warsaw, Poland
- <sup>73</sup> Niels Bohr Institute, Blegdamsvej 17, Copenhagen, Denmark
- <sup>74</sup> Niels Bohr Institute, Copenhagen University, Blegdamsvej 17, Copenhagen, Denmark
- <sup>75</sup> Nordita (Nordic Institute for Theoretical Physics), Roslagstullsbacken 23, SE-106 91 Stockholm, Sweden
- <sup>76</sup> SISSA, Astrophysics Sector, via Bonomea 265, 34136, Trieste, Italy
- <sup>77</sup> SMARTTEST Research Centre, Università degli Studi e-Campus, Via Isimbardi 10, Novedrate (CO), 22060, Italy
- <sup>78</sup> School of Physics and Astronomy, Cardiff University, Queens Buildings, The Parade, Cardiff, CF24 3AA, U.K.
- <sup>79</sup> Sorbonne Université-UPMC, UMR7095, Institut d'Astrophysique de Paris, 98 bis Boulevard Arago, F-75014, Paris, France
- <sup>80</sup> Space Research Institute (IKI), Russian Academy of Sciences, Profsoyuznaya Str, 84/32, Moscow, 117997, Russia
- <sup>81</sup> Space Sciences Laboratory, University of California, Berkeley, California, U.S.A.
- <sup>82</sup> Special Astrophysical Observatory, Russian Academy of Sciences, Nizhnij Arkhyz, Zelenchukskiy region, Karachai-Cherkessian Republic, 369167, Russia
- <sup>83</sup> Sub-Department of Astrophysics, University of Oxford, Keble Road, Oxford OX1 3RH, U.K.
- <sup>84</sup> The Oskar Klein Centre for Cosmoparticle Physics, Department of Physics, Stockholm University, AlbaNova, SE-106 91 Stockholm, Sweden
- <sup>85</sup> UPMC Univ Paris 06, UMR7095, 98 bis Boulevard Arago, F-75014, Paris, France
- <sup>86</sup> Université de Toulouse, UPS-OMP, IRAP, F-31028 Toulouse cedex 4, France
- <sup>87</sup> University Observatory, Ludwig Maximilian University of Munich, Scheinerstrasse 1, 81679 Munich, Germany
- <sup>88</sup> University of Granada, Departamento de Física Teórica y del Cosmos, Facultad de Ciencias, Granada, Spain
- <sup>89</sup> University of Granada, Instituto Carlos I de Física Teórica y Computacional, Granada, Spain
- <sup>90</sup> W. W. Hansen Experimental Physics Laboratory, Kavli Institute for Particle Astrophysics and Cosmology, Department of Physics and SLAC National Accelerator Laboratory, Stanford University, Stanford, CA 94305, U.S.A.
- <sup>91</sup> Warsaw University Observatory, Aleje Ujazdowskie 4, 00-478 Warszawa, Poland

## Appendix A: Polarization systematics

For both *Planck* instruments, the dominant polarization systematic in the published maps is the leakage of total intensity signal into polarized intensity due to the bandpass mismatch, i.e., the small differences in the bandpasses of the different detectors used to measure orthogonal polarization orientations. See [Planck Collaboration II \(2016\)](#) and [Planck Collaboration VII \(2016\)](#). This appendix discusses how we can characterize the effects and, in the case of HFI, compare the different methods used to correct it. The leakage is largest in the Galactic plane, since it is proportional to the total intensity. It is also *proportionately* worst in the plane due to the lower polarization fraction. Away from the plane, our analysis is not significantly affected, and here we estimate the effects in the plane.

### Appendix A.1: LFI

The LFI leakage is discussed in [Planck Collaboration II \(2016\)](#). The results along the Galactic plane are shown in [Fig. A.1](#) in comparison with the two low-frequency bands from WMAP. The comparison of the two WMAP bands gives an idea of the uncertainty in their correction, and the LFI 30 GHz data appear to deviate more than this. This is not unexpected given that the WMAP scan pattern allows the blind separation of the leakage, which is more difficult for LFI. In the inner Galactic plane, therefore, we should consider an additional systematic error of around 0.06 mK.

Though it is likely that the WMAP data are less affected by leakage along the Galactic plane, the WMAP solution has a high degree of uncertainty in its largest-scale modes, as discussed in [Page et al. \(2007\)](#). As a result, its high-latitude, large-scale morphology, where the signal is low, is unreliable, and it is there that the LFI data are more likely to be accurate. This issue is discussed in more detail in [Planck Collaboration X \(2016\)](#), which outlines the difficulties in measuring the largest-scale modes of the polarization signal for both *Planck* and WMAP. The cosmological analysis at high latitudes is far more sensitive to these issues than our analysis of the relatively high signal-to-noise Galactic foregrounds near the plane. Since we do not perform a quantitative fitting in this work, it is sufficient that we compare the data and model morphologies and use these comparisons when judging the significance of the residuals.

We take the rms variation among the three measures of the synchrotron emission (at 23 GHz, 30 GHz, and 33 GHz) as an estimate of the uncertainty shown by the grey band in the top panel of [Fig. A.1](#). These uncertainties in  $Q$  and  $U$  are then propagated to polarized intensity and shown as the grey band in [Fig. 5](#).

## Appendix A.2: HFI

There are two different leakage corrections included in the HFI data release. The default correction for HFI is based on the ground measurements of the bandpasses. The limitations of this method are mainly the accuracy of those measured bandpasses and the necessary assumption that the dust spectral index and temperature are constant over the sky. An alternative method is also discussed in [Planck Collaboration VIII \(2016\)](#) that performs a generalized global fit to correct for not only this bandpass leakage but also for calibration and monopole leakage.

In order to assess the two correction methods, we have looked at the three polarization frequencies of 143, 217, and 353 GHz (excluding 100 GHz, which is dominated by CO leakage that is an additional complication at this frequency but less important in the other frequencies). We extrapolate the different bands to a common frequency in order to compare them with each other. The variation among the bands may be due to spectral variation in the polarized emission but is more likely due to the bandpass leakage, which is significant on the inner Galactic plane where the total intensity is highest. We then compare these variations for the two corrections to determine if one is apparently better than the other, and we find that though they perform differently in different regions, they perform similarly overall.

In [Fig. A.1](#), we look at the Galactic plane profile at 353 GHz. The black curve shows the WMAP 94 GHz data for comparison, with a grey band showing its variation among the different years. These are extrapolated to 353 GHz using the *Planck* dust model spectrum of [Planck Collaboration XI \(2014\)](#). Though WMAP can solve for the leakage directly, there is a problem discussed by [Page et al. \(2007\)](#) with the largest-scale modes, which tend to be ill-constrained, an effect that contributes to the grey band indicating the variance among the different years. The dark blue curve represents the average of the three HFI frequencies 143, 217, and 353 GHz, each with the ground-based leakage correction applied. The pale blue band then shows the effective uncertainty in the dust polarization profile along the plane computed simply as the variation among the frequencies from their mean. We examined the same profiles for the alternate correction (not shown) and found that again, while the different corrections are better or worse in different places, neither is significantly better overall.

[Planck Collaboration X \(2016\)](#) quote an uncertainty of  $1 \mu\text{K}$  in the polarization at 353 GHz. [Figure A.1](#) shows that this estimate is of the right order on average.

We therefore use for our dust polarization data set the 353 GHz frequency band, which maximizes the signal-to-noise, with the ground-based bandpass correction applied. We estimate the systematic uncertainty using the variation among the frequencies, i.e., the pale blue bands in [Fig. A.1](#). The uncertainties in  $Q$  and  $U$  are then propagated to polarized intensity and shown as the grey band in [Figs. 12](#) and [14](#).

## Appendix B: Comparison of synchrotron emission estimates

We compare the data sets used to develop the magnetic field models in the literature discussed in [Sect. 3.2](#) in [Fig. B.1](#).

Recall that the Sun10 and Jaffe13 models were developed in reference to the synchrotron total intensity from the 408 MHz map while the Jansson12 model was fitted to the WMAP MCMC synchrotron estimate at 23 GHz.<sup>20</sup> We plot all data sets at a common frequency of 30 GHz to match LFI. For the WMAP 23 GHz maps, the small difference in frequency makes the plot insensitive to the precise spectrum assumed, and we use a power law with an index (in brightness temperature) of  $\beta = -3$ . For extrapolating the 408 MHz map to microwave bands, however, the spectrum assumed has a large effect on the result, and we do not know its variations over the sky. We show the result of using  $\beta = -3.1$ , the effective spectrum of the assumed synchrotron spectral template used in the *Commander* component separation ([Planck Collaboration X 2016](#)).

Another important uncertainty is that of the offset in the 408 MHz map. [Haslam et al. \(1982\)](#) quote 3 K as the zero-level uncertainty, and the map contains both CMB and an unresolved extragalactic component. [Lawson et al. \(1987\)](#) find an offset of 5.9 K, including both CMB and extragalactic components, though the 3 K uncertainty still applies. The purple curve in [Fig. B.1](#) has this offset removed. We compare this curve with the *Planck Commander* solution described in [Planck Collaboration X \(2016\)](#). As described in that paper, the synchrotron solution follows the morphology of the 408 MHz map but with an independent offset determination from [Wehus et al. \(2014\)](#) of 9 K (consistent with the Lawson offset within the calibration uncertainty) and a frequency dependence from a GALPROP simulated CRL spectrum. (The 3 K uncertainty at 408 MHz is equivalent to a  $5 \mu\text{K}$  uncertainty at 30 GHz assuming  $\beta = -3.1$ .)

The *Planck Commander* solution includes the posterior rms uncertainty at each position, and for the synchrotron total intensity, this is at the 1% level. This uncertainty does not, however, take into account the simplicity of the model and the uncertainties in the energy spectrum that have a large effect on the microwave intensity model.

In polarization, the WMAP curve differs slightly from the *Planck* polarization data. As described by [Page et al. \(2007\)](#), the WMAP polarization processing can solve for the leakage of intensity, which strongly affects LFI in the Galactic mid-plane (see [Planck Collaboration II 2016](#)), but WMAP also has unconstrained large-scale modes that are significant away from the plane. We discuss this in [Appendix A](#). The effect of the slightly different treatment of the systematics is visible in the comparison of the *Commander* synchrotron versus the LFI 30 GHz polarization itself.

These plots make clear the differences in the data sets that could be used for modelling the Galactic magnetic fields and indicate that the results may vary significantly depending on which choices are made. The implications for the models in the literature are discussed in [Sects. 3.2](#) and [5](#).

The situation will soon be improved by the completion of surveys such as: the ongoing C-Band All Sky Survey (C-BASS<sup>21</sup>, [King et al. 2014](#) and references therein) to map

<sup>20</sup> The total intensity synchrotron estimate used by Jansson12 is the WMAP MCMC solution (R. Jansson, private communication). Specifically, they used the basic WMAP MCMC component separation method described by [Gold et al. \(2011\)](#), i.e., with a synchrotron power law with no steepening and without fitting any AME component (aka “spinning dust”).

<sup>21</sup> <http://www.astro.caltech.edu/cbass/>



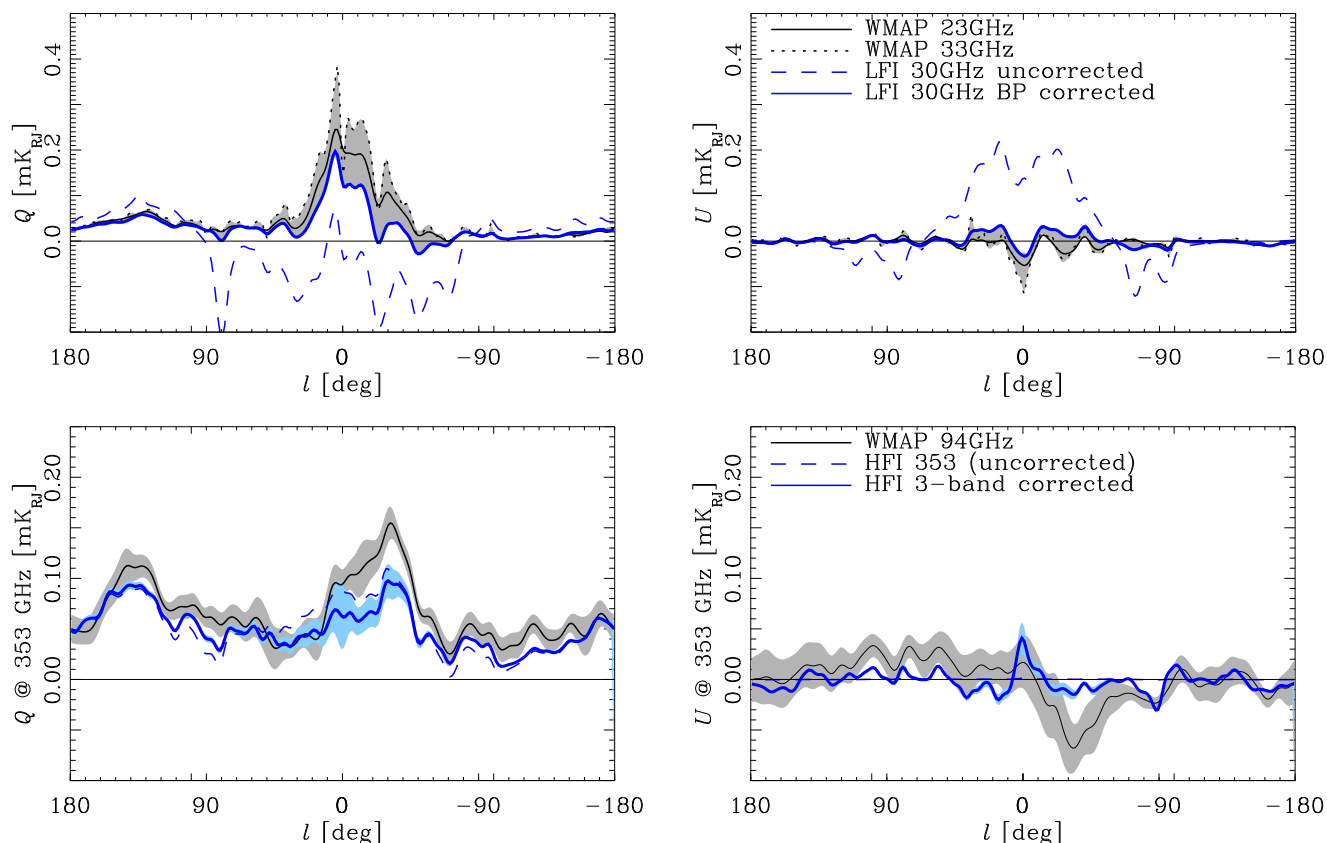


**Fig. A.1.** *Top:* comparison of LFI 30 GHz Stokes  $Q$  (left) and  $U$  (right) with WMAP 23 and 33 GHz along the Galactic plane smoothed to a full width half maximum (FWHM) of  $6^\circ$ . All frequencies are over-plotted by extrapolating the WMAP data to 30 GHz using a synchrotron  $\beta = -2.95$  (Jaffe et al. 2011). The grey band shows the rms variation among them. *Bottom:* average profile of three HFI frequencies with ground-based bandpass leakage correction. The 143 and 217 GHz frequencies are extrapolated to 353 GHz using the *Planck* dust model spectrum of Planck Collaboration XI (2014). The dark blue curve shows the average of the frequencies with a pale blue band showing the variance. The WMAP 94 GHz data are also extrapolated to 353 GHz in order to compare its profile in solid black with the grey band showing its variation among different years.

the full sky in polarization at 5 GHz; the S-band Parkes All-Sky Survey (S-PASS, Carretti et al. 2013) at 2.3 GHz; and the Q-U-I Joint Tenerife CMB Experiment (QUIJOTE, Génova-Santos et al. 2015 and references therein) planned for 10 to 40 GHz. These intermediate-frequency surveys will significantly advance our understanding of the synchrotron spectral variations and provide crucial frequencies for parametric component-separation algorithms like Commander.

## Appendix C: Model parameters

Table C.1 lists the changes to the magnetic field models. These models are extensively described in the references given, and we do not reproduce the full list here. Brief summaries of the models and methods used are given in Sect. 3.2. Any parameter not listed here retains its original value from the original references.

In Table C.2, we specify the dust model we use and list all of its parameters. This model is described in Sect. 4.

In Table C.3, we compare the CRL injection and propagation parameters in two GALPROP models: the one used in the analysis of Jaffe et al. (2011) on which Jaffe13 is based, and the one used for the results presented here.

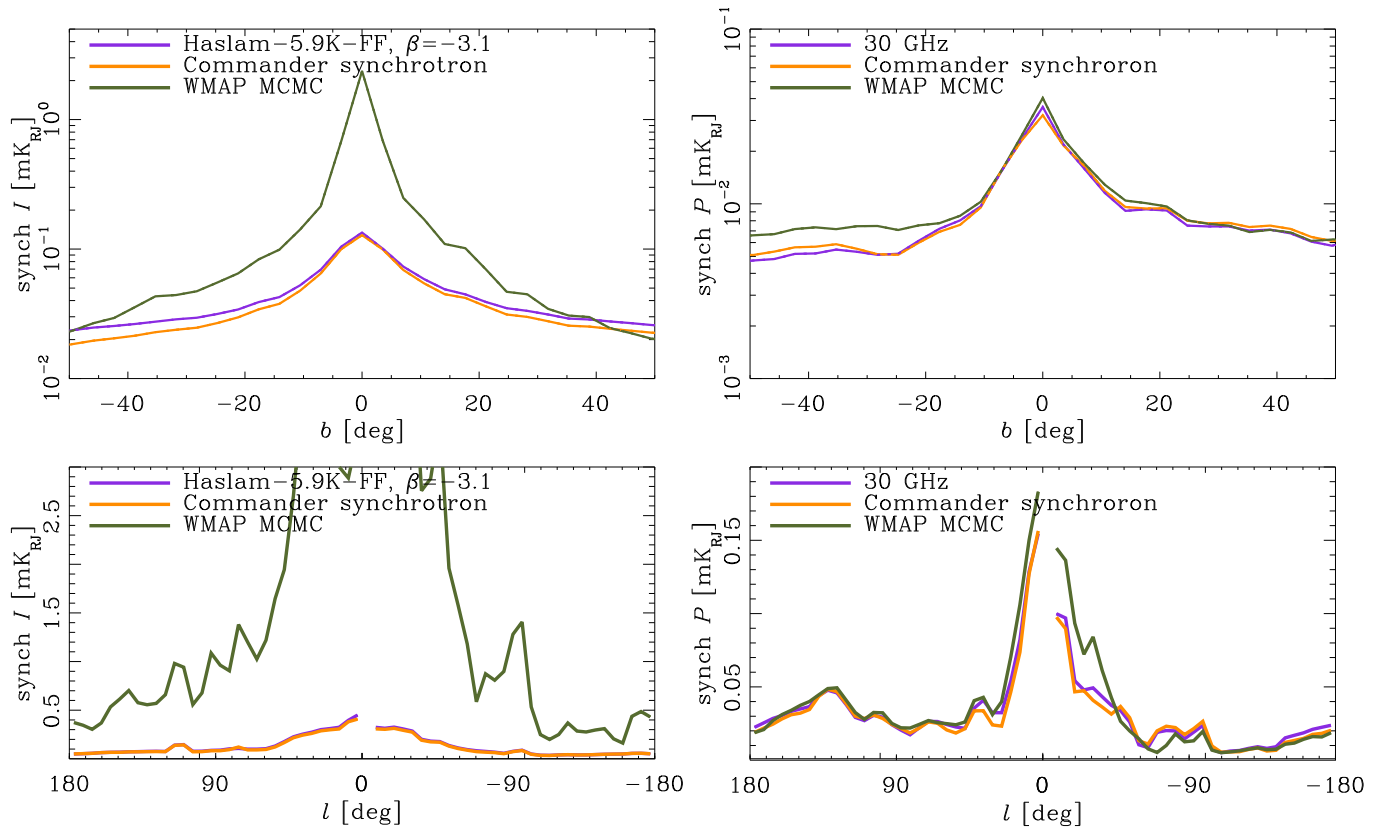


**Fig. B.1.** Comparison of synchrotron data sets as latitude (top) and longitude (bottom) profiles. For the latitude profiles, the full sky is averaged excluding the inner  $10^\circ$  ( $|b| < 10^\circ$  and  $|l| < 10^\circ$ ). For the longitude profiles, only the pixels along the plane are plotted. In total intensity on the left, the **Commander** synchrotron solution, which is identical (except for an offset) to the Haslam 408 MHz map, is compared to the WMAP MCMC synchrotron solution. In polarization, on the right, the **Commander** synchrotron is compared to the LFI 30 GHz map itself and the WMAP MCMC synchrotron solution extrapolated to 30 GHz assuming  $\beta = -3$ .

**Table C.1.** Parameter updates to models in the literature.

Model	Param.	Orig. value	New value	Comments
“Sun10b” Sun et al. (2008) Sun & Reich (2010)	$\langle B_{\text{iso}}^2 \rangle^{1/2}$	3 $\mu\text{G}$	6.4 $\mu\text{G}$	Increased random field component, degenerate with CRL normalization.
	$\beta$	...	3	
	$r_0^{\text{ran}}$	...	30 kpc	Uniform random field changed to combination of thin and thick exponential discs, i.e., $\mathbf{B}(z) \propto (1 - f_{\text{disc}}^{\text{ran}}) \text{sech}^2(z/h_{\text{halo}}^{\text{ran}}) + f_{\text{disc}}^{\text{ran}} \text{sech}^2(z/h_{\text{disc}}^{\text{ran}})$ , $\mathbf{B}(r) \propto \exp[-(r - R_{\odot})/r_0^{\text{ran}}]$ .
	$f_{\text{disc}}^{\text{ran}}$	...	0.5	
	$h_{\text{halo}}^{\text{ran}}$	...	3 kpc	
	$h_{\text{disc}}^{\text{ran}}$	...	1 kpc	
	$B_c$	2 $\mu\text{G}$	0.5 $\mu\text{G}$	Dropping the amplitude in the inner Galaxy so as not to overpredict.
“Jaffe13b” Jaffe et al. (2010, 2011, 2013)	$\langle B_{\text{iso}}^2 \rangle^{1/2}$	5 $\mu\text{G}$	6.5 $\mu\text{G}$	Reduced global normalization of isotropic random component, increasing field ordering. (Here defined at $r = R_{\odot}$ rather than at $r = 0$ .)
	$f_{\text{ord}}$	0.2	0.5	
	$a_i$	various	various	
	$h_{\text{disc}}$	6	0.1 kpc	Jaffe13 vertical profile not previously constrained. All components now with thin and thick discs. Random like Sun10 model above. Coherent: $B(z) = B_0^{\text{disc}} \text{sech}^2(z/h_{\text{disc}}) + B_0^{\text{halo}} \text{sech}^2(z/h_{\text{halo}})$ .
	$h_{\text{halo}}$	...	3 kpc	
	$h_c$	0.5 kpc	0.1 kpc	
	$B_0^{\text{halo}}$	...	1.38 $\mu\text{G}$	
	$B_0^{\text{disc}}$	...	0.17 $\mu\text{G}$	
	$h_{\text{halo}}^{\text{ran}}$	...	4 kpc	
	$h_{\text{disc}}^{\text{ran}}$	...	1 kpc	
	$r_0^{\text{ran}}$	20 kpc	12 kpc	
$f_{\text{disc}}^{\text{ran}}$	...	0.1	See Sun10 comment above.	
“Jansson12b” ordered fields Jansson & Farrar (2012a)	$b_6^{\text{disc}}$	-4.2	-3.5	Overpredicted outer Galaxy in the plane in total and polarized intensity. (Segment 6 is the Perseus arm.)
	$B_X$	4.6	1.8	Polarization overpredicted at high latitude.
	$\beta$	1.36	10	Changed strength of ordered random (“striated”) fields, adjusting for different CRL normalization.
“Jansson12b” random fields Jansson & Farrar (2012b)	$\langle B_{\text{iso}}^2 \rangle^{1/2}$	...	7.8 $\mu\text{G}$	Using a GRF simulation, the global normalization of all random components.
	$b_{\text{even}}^{\text{disc}}$	various	0.8	Replacing random field dominated by a single arm segment ( $b_7^{\text{disc}} = 37 \mu\text{G}$ ) with four roughly equal arms (even-numbered) and four inter-arm regions (odd-numbered).
	$b_{\text{odd}}^{\text{disc}}$	various	0.4	
	$b_{\text{int}}^{\text{disc}}$	7.63 $\mu\text{G}$	0.5	Values now relative to $\langle B_{\text{iso}}^2 \rangle^{1/2}$ .
	$B_0$	4.68 $\mu\text{G}$	0.94	When using the GRF scaled by $\langle B_{\text{iso}}^2 \rangle^{1/2}$ , maintain the same halo amplitude.
“Jansson12c” ordered fields as Jansson12b except:	$B_n$	1.4 $\mu\text{G}$	1 $\mu\text{G}$	Reducing the toroidal halo components that partly cancel the disc component; increasing x-shaped halo to compensate high-latitude synchrotron.
	$B_s$	-1.1 $\mu\text{G}$	-0.8 $\mu\text{G}$	
	$B_X$	1.8 $\mu\text{G}$	3 $\mu\text{G}$	
	$b_2^{\text{disc}}$	3 $\mu\text{G}$	2 $\mu\text{G}$	Reduce inner Galaxy dust polarization.
	$b_4^{\text{disc}}$	-0.8 $\mu\text{G}$	2 $\mu\text{G}$	Replacing synchrotron polarization.
	$b_5^{\text{disc}}$	-2 $\mu\text{G}$	-3 $\mu\text{G}$	Increase high-latitude polarization.
“Jansson12c” random fields as Jansson12b except:	$b_6^{\text{disc}}$	0.8	1.6	To increase outer-Galaxy synchrotron intensity in the plane.
	$b_{\text{odd}}^{\text{disc}}$	0.4	0.1	To compensate the above change on average. Then to further increase local high-latitude dust polarization, set only $b_5^{\text{disc}} = 0$ .
	shift	...	0.97	Shift the arm pattern by multiplying the $r_{-x}$ parameters from Jansson & Farrar (2012a) by this factor.

**Notes:** Where not specified, parameters remain at the values in the references. The notation of the original references is used for each model with added sub- or super-scripts as necessary to clarify different field components. (The Jansson12 parameter that controls the amount of power in ordered random fields relative to that of the coherent fields is  $\beta$ , not to be confused with the temperature spectral index, also  $\beta$  elsewhere in this work.)



**Table C.2.** Description of the model for the distribution of dust emissivity.

Param.	Default	Equation	Description
DISC COMPONENT			
$r_0$	6 kpc	$\rho(r) = \exp(-r/r_0)$	Exponential disc scale radius.
$z_0$	0.3 kpc	$\rho(z) = \text{sech}^2(z/z_0)$	Exponential disc scale height.
$R_{\text{max}}$	12 kpc	...	Maximum radius, beyond which $\mathcal{E}_{\text{dust}} = 0$ .
SPIRAL ARMS			
$R_{\text{mol}}$	5 kpc	...	Radius of molecular ring.
$a_i$	{4, 2, 1.5, 4, 2}	$\rho_{\text{arm},i} = a_i \rho_c(d_i)$	Amplitude of each of four spiral arms and molecular ring. Order corresponds to: Perseus, Sagittarius, Scutum, Norma, molecular ring. The Sagittarius arm is damped relative to the others, and the amplitudes are relative to the smooth background component.
		$\rho_c(d) = c(r)\rho_c(z)\rho(r)\exp(-(d/d_0(r))^2)$	Amplification factor relative to background. $d$ is the distance along Galacto-centric $\hat{r}$ to the nearest arm in kpc, computed using $r_i(\phi)$ .
$\phi_{0,i}$	$70^\circ + 90^\circ i$	$r_i(\phi) = R_s \exp[(\phi - \phi_{0,i})/\beta]$ and $\beta \equiv 1/\tan(\theta_p)$	$r(\phi)$ gives the arm radius at a given azimuth, where $\phi_{0,i}$ is the azimuthal orientation of the spiral around the axis through the Galactic poles. (Constant $R_{\text{mol}}$ for molecular ring.)
$\theta_p$	$-11^\circ.5$	...	Pitch angle of the spiral arms
$C_0$	5.7	$c(r) = \begin{cases} C_0 & \text{if } r \leq r_{\text{cc}} \\ C_0(r/r_{\text{cc}})^{-3} & \text{if } r > r_{\text{cc}} \end{cases}$	Arm amplitude relative to inter-arm, tailing off after $r_{\text{cc}}$ .
$r_{\text{cc}}$	9 kpc	...	Region of constant arm amplification.
$d_0$	0.1 kpc	$d_0(r) = d_0/(c(r)\rho(r))$	Defines the base width of arm enhancement, which varies with radius.
$h_c$	0.04 kpc	$\rho_c(z) = \text{sech}^2(z/h_c)$	Scale height of the spiral arm component.
LOCAL BUBBLE			
$R_{\text{LB}}$	150 pc	...	Radius of cylindrical region about the observer.
$h_{\text{LB}}$	200 pc	...	Height of cylindrical region about the observer.
$a_{\text{LB}}$	0	$A = \begin{cases} 1 & \text{if } r_{\odot} > R_{\text{LB}} \text{ and }  z  > h_{\text{LB}} \\ a_{\text{LB}} & \text{if } r_{\odot} \leq R_{\text{LB}} \text{ and }  z  \leq h_{\text{LB}} \end{cases}$	Relative amplitude within the local bubble.

**Notes:** See Sect. 4.1. The model is a smooth exponential disc plus four logarithmic spiral arms that have a Gaussian density profile as a function of radius from the arm ridge:  $\mathcal{E}_{\text{dust}} \propto A [\rho(r)\rho(z) + \sum_i^{N_{\text{arms}}} \rho_{\text{arm},i}]$ .

**Table C.3.** Comparison of the CRL injection and diffusion parameters.

Parameter	z04LMPDS	z10LMPD
$ z _{\max}$ [kpc] . . . . .	4	10
D0_xx . . . . .	$3.4 \times 10^{28}$	$6 \times 10^{28}$
electron_norm_Ekin [MeV] . . .	$3.45 \times 10^4$	$3.45 \times 10^4$
electron_norm_flux . . . . .	$0.3 \times 10^{-9}$	$0.3 \times 10^{-9}$
[( $\text{cm}^2 \text{ sr s MeV}$ ) $^{-1}$ ]		
electron_g_0 . . . . .	{1.3, 1.6, 1.8} <sup>a</sup>	1.6
electron_rigid_br0 [MV] . . . . .	$4 \times 10^3$	$4 \times 10^3$
electron_g_1 . . . . .	2.25	2.5
electron_rigid_br [MV] . . . . .	...	$5 \times 10^4$
electron_g_2 . . . . .	...	2.2

<sup>a</sup> The low-energy injection index was 1.8 in [Strong et al. \(2010\)](#), the preferred value in [Strong et al. \(2011\)](#) was 1.6, and Jaffe13 used the fitted value of 1.3 from [Jaffe et al. \(2011\)](#).

**Notes:** z04LMPDS from [Strong et al. \(2010\)](#) was used in Jaffe13, while the newer model z10LMPD from Orlando13 was used as the base model for the synchrotron spectral template in **Commander** as described in [Planck Collaboration X \(2016\)](#), and it is the common model we use for all results presented here. See [Sect. 3.1](#) for discussion.